Investigating the Impacts of Bin Variability on Particle Size Distributions in Multiphase Eulerian-Eulerian Simulations

Wilbert Alexander Cruz
Marquette University

INVESTIGATING THE IMPACTS OF BIN VARIABILITY ON PARTICLE SIZE DISTRIBUTIONS IN MULTIPHASE EULERIAN-EULERIAN SIMULATIONS

by

Wilbert A. Cruz, B.S.

A Thesis submitted to the Faculty of the Graduate School,
Marquette University,
in Partial Fulfillment of the Requirements for
the Degree of Master of Science

Milwaukee, Wisconsin

May 2024

ABSTRACT

INVESTIGATING THE IMPACTS OF BIN VARIABILITY ON PARTICLE SIZE DISTRIBUTIONS IN MULTIPHASE EULERIAN-EULERIAN SIMULATIONS

Wilbert A. Cruz, B.S.

Marquette University, 2024

In this study, a 3D steady-state Eulerian-Eulerian simulation was developed to investigate flow performance in a dilute pneumatic conveying system. The investigation focused on two main objectives: (1) assessing the influence of bin selection on solution accuracy for representing the polydisperse mixture, and (2) exploring methods to simplify the modeling of polydisperse particles in the simulation by utilizing a mean diameter derived from the mixture's particle size distribution. The system's geometry and initial boundary conditions featured a 10.6 m long, 150 mm diameter horizontal pipe with both gaseous and solid phases initially moving at $27\frac{\mathrm{m}}{\mathrm{s}}$. The steady-state simulation replicated an experimental pneumatic conveying system built by Laín and Sommerfeld, to compare and validate the proposed Eulerian-Eulerian model with experimental data.

The dilute mixture used in this study mirrored Laín and Sommerfeld's particle size distribution (PSD), consisting of particle diameter sizes of approximately 15 μm to 85 μm. By incorporating an inhomogeneous discrete population model, a set of five bin cases were conducted using Laín's PSD in the Eulerian-Eulerian simulation. An additional monodisperse case was examined, featuring particle sizes of 40 μm which corresponded to Laín and Sommerfeld's PSD mean diameter. This comparison aimed to evaluate the efficacy of representing the polydisperse mixture via bin characterization techniques, as opposed to utilizing a single mean diameter from the PSD.

After validating the model, a series of four PSDs, ranging from 5 μm to 500 μm, were examined. Bin convergence studies were conducted for each PSD, as well as the viability of utilizing mean diameter expressions to represent each particle size distribution was investigated. Through this study, it was found that approximately 20 bins were necessary to accurately capture the pressure profiles of the system for most PSDs. Furthermore, simulations utilizing particle sizes based on the Sauter mean diameters demonstrated the most favorable agreement in pressure drop predictions, showcasing up to 0.086% deviations with highest bin cases. The remaining mean diameter expressions gave rise to similar system pressure drop values, with De Brouckere being the second most accurate, and volume mean, surface area mean and arithmetic mean diameters following respectively.

ACKNOWLEDGEMENTS

Wilbert A. Cruz, B.S.

I would like to acknowledge Dr. Casey for his amazing mentorship during the entire thesis process. His guidance and participation in conferences have enhanced my research presentation skills and played a pivotal role in shaping my academic journey. I sincerely appreciate his expertise and unwavering support, and I am truly thankful for the numerous opportunities he has given me to learn and grow under his mentorship.

I would like to express my sincere appreciation to Dr. Singer for his insightful advice on optimizing my simulation models. Dr. Singer's mentorship has not only enriched my understanding of simulation methodologies but has also contributed significantly to the overall quality of my research.

Special acknowledgment goes to Dr. Bowman for his incredible insights into ANSYS CFD models and for the skills I acquired through his HVAC course. I am grateful for all the opportunities I have had to engage in meaningful conversations with him and for all the knowledge I gained under his instruction.

I would like to mention Marquette University for providing me with the essential tools and resources that have been instrumental in the successful completion of my mechanical engineering thesis. I am also grateful for the opportunities for learning and growth that Marquette University has offered me.

Furthermore, I extend my thanks to my fellow mechanical engineering graduate students for their companionship throughout this academic journey. I appreciate the sense of unity and collaboration among the mechanical engineering graduate students.

Lastly, I extend my deepest gratitude to my parents, their hard work and dedication have been the cornerstone of my academic journey. Their belief in my abilities, constant encouragement, and sacrifices have provided me with the foundation to pursue my academic goals. My accomplishments reflect their enduring belief in my potential, and for that, I am truly grateful.

TABLE OF CONTENTS

LIST OF TABLES

LIST OF FIGURES

LIST OF EQUATIONS

LIST OF ABBREVIATIONS

C_d	Drag coefficient
C_l	Lift Coefficient
N	Total number of phases
Re_ω	Reynolds number based on vorticity
Re_s	Particle's Reynolds Number
d_s	Particle Diameter
K_{pq}	Fluid-Solid Exchange Coefficient between Phase q and Phase p
α_q	Volume fraction of Phase q
ρ_q	Density of Phase q
v_q	Velocity of Phase q
v_p	Velocity of Phase p
g	Acceleration due to gravity
μ	Viscosity
St	Stokes' Number
$\dot{m}_{pq}$	Mass transfer from phase p to phase q
p	Pressure
p_s	Solids Pressure of s^{th} solid phase
$\bar{\bar{\tau}}_s$	Solids Shear Stress
$\vec{R}_{pq}$	Interphase Force between Phase q and Phase p
$\vec{F}_q$	External Body Force Phase q

$F_{lift,q}$	Lift fore of Phase q
$F_{vm,q}$	Virtual Mass Force of Phase q
$\vec{F}_{wl,q}$	Wall lubrication force of Phase q
$\vec{F}_{td,q}$	Turbulent dispersion force of Phase q
μ_s	Solid Shear Stress
$\mu_{s,col}$	Collisional Viscosity
$\mu_{s,kin}$	Kinetic Viscosity
$\mu_{s,fr}$	Frictional Viscosity
τ_s	Particle Relaxation Time
St	Stokes Number
g_0	Radial Distribution Function
$\alpha_{s,max}$	Maximum Packing Limit
Θ_s	Granular Temperature
e_{ss}	Coefficient of restitution between particles
e_{sw}	Coefficient of restitution between particles and wall
φ_{ls}	Transfer of Kinetic Energy due to phase velocity fluctuations
β	Saffman-Mei Dimensionless Parameter
$\bar{\bar{I}}$	Identity Tensor
$\vec{U}_{s,\|}$	Particle slip velocity parallel to the wall
ϕ	Specularity Coefficient
q_s	Heat flux
$x_{i,j}$	Spatial Cartesian Coordinates for position

$u_{i,j}$	Spatial Cartesian Coordinates for velocity
μ_{eff}	Effective viscosity
k	Turbulent Kinetic Energy
ε	Turbulent Dissipation Rate
$S_{k,\varepsilon,\alpha_p}$	Source Terms
Y_M	Contribution of Fluctuating Dilatation
$\alpha_{k,\varepsilon}$	Inverse effective Prandtl Numbers
G_k	Generation of Turbulence Kinetic Energy due to Velocity Gradient
G_b	Generation of Turbulence Kinetic Energy due to Buoyancy
S_{bi}	Net Mass Source Term
f_i	Discrete bin fraction
$\vec{u}_p$	Velocity of Phase p
V	Cell Volume
U_f^n	Volume flux through the face of the cell at time step n
$\alpha_{q,f}^n$	Face value of the q^{th}phase volume fraction at time step n
α_q^n	Cell value of volume fraction at time step n
f_p	Particle Mass Flux
R	Pipe Radius
U_s	Particle velocity
U_{av}	Effective Particle Velocity
f_p	Effective Particle Mass Flux
D	Pipe Diameter
L	Pipe Length

I. INTRODUCTION

A. CFD Modeling in Pneumatic Conveyors

The designing process of pneumatic conveying systems is a critical aspect in various industries, where the efficient transport of bulk materials through pipelines is essential for a wide variety of manufacturing processes. Manufacturing industries heavily rely on these systems to efficiently move granular and powdered materials, emphasizing the importance of ensuring that pneumatic conveyor systems are designed accordingly by considering the interactions between material properties, system geometry, and the operational conditions the systems sustain.

The intricacies of designing an effective pneumatic conveyor involve meticulous consideration of several parameters to optimize material handling. In particular, parameters such as particle size, shape, and density significantly influence material behavior within the conveying system [1]. To comprehend how a pneumatic conveyor design might be affected by the material behavior experienced throughout the conveying process, computational fluid dynamic models (CFD) are employed to further understand the solid-fluid multiphase interactions involved.

By using CFD models, predictions and considerations can be made regarding the granular particle behavior and its influence on the system. Important particle effects that need to be considered when designing these systems include friction, conveying velocities, pressure drop induced by the granular phase and concentration distributions within the flow [2]. The ability to predict these effects using CFD models proves valuable

in the designing process by eliminating the need of developing largely scaled experimental prototypes to fully comprehend the multiphase flow behavior in the system. Through this approach, pneumatic conveying systems can be designed properly, ensuring their resilience and their ability to withstand the effects predicted during operation.

In contrast to traditional physical and experimental testing methods, which rely on real-time data gathering for direct validation, the computational modeling approach stands out with its considerable advantages. Unlike the economically expensive and resource-intensive nature of physical testing, computational modeling proves to be cost-effective, requiring minimal setup and possessing the ability to overcome geometric size limitations when simulating the system. Furthermore, CFD approaches can provide more detailed information on flow behavioral patterns and can expedite the data gathering process. It is important to note, however, that while computational models offer these benefits, their accuracy and reliability still necessitate validation to some extent through experimental testing.

The validation process for CFD models is often achieved by conducting tests on a smaller-scaled replica of the system of interest. Through geometric, kinematic, and kinetic similarity, the validated simulated model can then be upscaled to accurately represent the larger system [3-5]. If the model is successfully validated for the smaller system, the similarity relationships can be applied and subsequently evaluated, thereby removing the need for an extensive and costly, larger-scale experimental setup. For this study, the proposed Eulerian-Eulerian model was validated using experimental data gathered by Laín and Sommerfeld [6], to validate the modeled pressure drop, particle velocity and mass flux solutions for the pneumatic conveying system.

B. Laín and Sommerfeld Pneumatic Conveying Study

The studies conducted by Laín and Sommerfeld [6] and Huber and Sommerfeld [7] investigate the transport of solid particles in an experimental pneumatic conveying system. In the investigation conducted by Laín and Sommerfeld, the experimental configuration consisted of stainless steel horizontal and vertical pipes. This experimental setup was used for exploring crucial parameters, including particle velocities, pressure drop and mass fluxes of the solid phase through the pipes.

The geometry proposed by Laín and Sommerfeld featured a 150 mm pipe diameter and an 8 m horizontal pipe length. For the air flow component, Laín and Sommerfeld employed a roots blower capable of achieving a maximum flow rate of $0.15\ \frac{\mathrm{m}^3}{\mathrm{s}}$ and a maximum backpressure of 0.2 bar. This configuration allowed for the variation of transport velocities from $10\frac{\mathrm{m}}{\mathrm{s}}$ to $30\frac{\mathrm{m}}{\mathrm{s}}$ and for the accommodation of particle loadings up to $2\ \frac{\mathrm{kg\ dust}}{\mathrm{kg\ air}}$. The solid particles utilized in their research comprised a polydisperse mixture of spherical glass beads, featuring a density of $2500\frac{\mathrm{kg}}{\mathrm{m}^3}$ and a number mean diameter of approximately 40 μm. For solution data extraction, Laín and Sommerfeld collected particle velocity and mass flux data perpendicular to the flow, and collected pressure drop data parallel to the flow. Their experiment yielded valuable insights into the intricate dynamics of pneumatic conveying systems, particularly focusing on the effects of bends in the pipe and the characteristics of particle distributions in the mixture. In addition to their findings, they employed their experimental results to validate the Eulerian-Lagrangian modeling approach used to simulate their dilute-flow case.

Based on their detailed investigation, the horizontal pipe framework used in their study was replicated in this report to create a series of Eulerian-Eulerian simulations. These simulations incorporated identical boundary conditions, geometry, meshing, and sizing techniques as those used in their Eulerian-Lagrangian model. The simulated pipe, as outlined by Huber and Sommerfeld [7], retained a diameter of 150 mm, a length of 10.6 m, and a mean conveying velocity of $27\,\frac{\mathrm{m}}{\mathrm{s}}$ for both phases. Similarly, a vertical profile was established for data extraction at a point 8m from the inlet boundary. The material properties for the fluid phase, including the density and dynamic viscosity of air, were defined at approximately $1.2\,\frac{\mathrm{kg}}{\mathrm{m}^3}$ and $18.0\,\times\,10^{-6}\,\frac{\mathrm{kg}}{\mathrm{m}\cdot\mathrm{s}}$ respectively. In addition to the gaseous phase, the simulation characterized the particle phase by integrating the same properties of the experimental glass beads utilized in Laín and Sommerfeld's study. To further characterize the polydisperse mixture utilized in both studies, their particle size distribution, extracted from a continuous cumulative distribution, was digitized and employed for model validation. With these parameters, the accuracy of the proposed Eulerian-Eulerian model could be assessed against the empirical data obtained from the studies conducted by Laín, Sommerfeld, and Huber.

C. Applicability of the Eulerian-Eulerian Modeling Approach

Within the available computational models, the Eulerian-Eulerian model's versatility proves to be ideal for simulating dilute and dense granular flows for pneumatic conveying systems. Sarrami [8] validated the model's ability to predict pressure drop for both flow regimes by comparing it against experimental data. Sarrami found substantial quantitative agreement in pressure drop profiles between simulated results and dense-flow experimental trials, with a mere 1% difference in solution data observed for the dense case. However, in dilute-phase conveying simulations, the pressure drop was underestimated by approximately 20%, although this disparity was reported to be within acceptable error ranges for this flow regime. Santosh's study [9] similarly aimed to compute pressure drop for a gas-solid, two-phase flow within a horizontal pipe. The granular concentration studied fell within the upper limit of the dilute phase flow regime, with the solid volume fraction of the mixture ranging from 1% to 10% of the total mixture. Utilizing these concentrations, Santosh reported a 2.7% agreement of the Eulerian-Eulerian model in simulating the pressure drop of his pneumatic system.

The versatility of the Eulerian-Eulerian modeling approach highlighted in these studies stems from its ability to treat solid and fluid phases as continuous entities, incorporating a strategic pseudo-fluid treatment for the solid phase. This treatment enabled the utilization of volume-averaged equations for both phases, providing a simplified yet effective method for simulating dense and dilute granular flows. Through the Eulerian-Eulerian model's averaging process, conservation equations for mass, momentum, and energy could be solved for both solid and fluid phases in each cell throughout the computational domain.

The CFD simulations in this study were developed using ANSYS Fluent, a leading software tool for fluid dynamics analysis and simulation. Within ANSYS Fluent, the Eulerian-Eulerian model is available for simulating granular multiphase flows. However, to effectively utilize the Eulerian-Eulerian model, it is imperative to establish the necessary models needed to accurately describe the behavior of both the gaseous and solid phases within the flow. These models should capture key phenomena such as particle motion, collision, and interactions with the surrounding fluid. By incorporating the necessary models required to accurately describe phase interactions in the flow, the Eulerian-Eulerian approach can be effectively used to simulate the investigated pneumatic conveying system.

D. Granular Model Studies for Eulerian-Eulerian Simulations

The simplified phase description of the Eulerian-Eulerian model enables it to produce accurate results while remaining computationally efficient, rendering it particularly advantageous for modeling complex particulate flows. In contrast to more computationally demanding models like the Eulerian-Lagrangian approach, which tracks each particle individually, the Eulerian-Eulerian approach provides a valuable alternative that offers comparable accuracy and remains better suited for simulating larger-scale dense systems.

Eulerian-Lagrangian models encounter several challenges when simulating dense flows with high collision frequencies among particles. These challenges arise from the computational complexity and intensity required for establishing coupling schemes [10].

The Eulerian-Eulerian approach can bypass these difficulties by simulating the particulate phase as a fictitious fluid, representing the fluid dynamic behavior of the collection of particles. For this reason, the Eulerian-Eulerian approach has become valuable in accurately representing complex pneumatic conveying scenarios without the intensive computational demands associated with representing and tracking each individual particle. By incorporating the Kinetic Theory of Granular Flows (KTGF), the model can further describe interactions between the gaseous and particle phases, such as collisions, friction, cohesion, compression, expansion, momentum transfer, and clustering [11].

According to the KTGF, there are multiple important granular properties that must be considered to accurately represent the particle behavior experienced in the flow. Within these parameters, particle drag, granular viscosity, granular temperature, solids pressure, radial distribution functions and more need to be considered.

In prior research exploring the applicability of these models, Konstantin [12] examined the variance in drag correlation for gas-solid flows. Konstatin discovered that the Wen-Yu [24] and Gidaspow [15] models showed better alignment with experimental data, particularly for flows characterized by low Reynolds numbers. Mukesh [13] supported this assertion in his study on fluidized beds, where he examined various drag correlations similar to Konstantin. Mukesh found significant agreement between simulation results and experimental data for solid profiles when using drag models like Syamlal-O'Brien, Gidaspow, Wen-Yu, and Huilin-Gidaspow, resulting in Root Mean Square Error (RMSE) values ranging from 0.022 to 0.0245.

In the ANSYS Fluent Theory Manual, which discusses all modeling techniques available for various fluid applications, the Wen-Yu drag model is recommended for

describing dilute flow regimes where the volume fractions of the solid phase consist of less than 1% of the mixture [14]. Apart from drag correlations, ANSYS Fluent provided granular viscosity, temperature, conductivity, solids pressure, radial distribution functions, and boundary condition models for granular temperature at the wall, which were required to accurately simulate the system. Gidaspow provided correlations for defining granular viscosity, temperature, and conductivity through his multiphase flow and fluidization studies of circulating fluidized beds, which were proven to be accurate for simulating the flow regime targeted in this study [15-17]. Lun et. al [14] solids pressure and radial distribution functions were able to describe the minimal particle-particle effects for the dilute flow, and the Johnson and Jackson's [19] granular wall temperature model has been widely successful for simulating Eulerian-Eulerian solid-gas flows within this regime [18-19]. By utilizing these models, the solid phase and its effects on the gaseous phase could be predicted accordingly.

Apart from literature, preliminary sensitivity studies were conducted to assess the impact of these models on pressure drop, velocity profiles, and volume fraction solutions within the simulated pneumatic conveyor, ensuring alignment with previously cited works. The sensitivity study results, consistent with literature, are detailed in Appendix B. In addition to the chosen granular models, it was crucial to incorporate a population balance modeling technique capable of accurately describing the polydisperse nature of the flow.

E. Population Balance Models in Eulerian-Eulerian Modeling

Other advantages of the Eulerian-Eulerian model when simulating polydisperse solid-fluid multiphase flows include its ability to represent particle size distributions through population balance models. Among these, the inhomogeneous discrete modeling approach can discretize the particle size distribution into a series of bins within the simulation. Each bin represents an average particle size calculated from a set of particle size ranges in the distribution. Independent mass and momentum equations are solved for each bin, giving rise to variations in particle behavior contingent on the particle size ranges prescribed to each bin. In this way, pressure, velocity and concentration dispersion effects can be studied individually for each bin within the polydisperse mixture. By adopting the inhomogeneous discrete method, the model can capture the intricate dynamics of real polydisperse multiphase flows observed in pneumatic conveyors. Thus, it is crucial to characterize the polydisperse mixture via a population model to accurately represent the system.

Some examples of Eulerian-Eulerian studies describing polydisperse mixtures for multiple applications, such as Hassan's water and oil two-phase numerical modeling [20], Kharoua's horizontal three-phase separator [21] and Siamak bubbly flow columns analysis [22], incorporate population balance models to characterize a desired phase distribution. Most studies that use population balance models to discretize the particle size distribution (PSD) into a set of bins assume that using a higher number of bins to represent the polydisperse mixture will always give rise to the most optimized results. However, there have been limited quantifiable publications addressing how to select the optimal number of bins that could still give rise to highly accurate results, while

consuming a significantly lower number of computational resources. Furthermore, alternatives for representing the PSD as a monodisperse mixture to reduce the complexity of the model by using mean diameter particle sizes such as Sauter Mean, De Brouckere, arithmetic mean, surface area mean, and volume mean have not been thoroughly investigated in literature.

Following this line of reasoning, the primary focus of this research is to investigate how pressure drop solution accuracy varied when employing various modeling techniques to depict the polydisperse mixture within the simulated pneumatic conveying system. By applying the Eulerian-Eulerian modeling approach, this study focused on (1) varying the number of bins representing the PSD used in the population balance model to investigate bin convergence, and (2) finding alternative methods of representing the PSD via a mean diameter expression that would still give rise to satisfactory results. In this manner, this investigation aims to offer a viable and simplified modeling technique that could be used to describe complex polydisperse mixtures in pneumatic conveying flow systems.

II. NUMERICAL METHODS

A. Transport Equations

To implement the proposed Eulerian-Eulerian simulation, the numerical scheme employed to model the solid-gaseous flow followed an implicit numerical scheme in which the volume fraction equations were discretized. The implicit scheme operated by simulating the volume fraction at the current time step as a function of various flow parameters at the same time step. This approach enabled scalar transport equations to be iteratively solved for each secondary-phase volume fraction in the simulation [14]. The discretized volume fraction for phase *q* was represented as shown in Equation 1, where *n* represents the index of the previous time step and *n+1* the index of the current time step:

$$\frac{\alpha_q^{n+1}\rho_q^{n+1}-\alpha_q^n\rho_q^n}{\Delta t}V+\sum_f\left(\rho_q^{n+1}U_f^{n+1}\alpha_{q,f}^{n+1}\right)=\left[S_{\alpha_p}+\sum_{p=1}^{n}\left(\dot{m}_{pq}-\dot{m}_{qp}\right)\right]V \quad (1)$$

Apart from the numerical scheme used, the Eulerian-Eulerian modeling technique selected treated both phases, the primary gaseous air phase and secondary solid glass-beads phase, as interpenetrating continua [10]. By employing this approach, both phases were able to coexist, interact, and move within the same computational domain simultaneously. In this manner, a set of Navier-Stokes equations could be solved independently for each phase. By employing the Navier-Stokes momentum equations, the following general momentum balance was formulated for phase *q* as:

(2) $$\frac{\partial}{\partial t}\left(\alpha_q \rho_q\right) + \nabla \cdot \left(\alpha_q \rho_q \vec{v}_q \vec{v}_q\right) = -\alpha_q \nabla p + \nabla \cdot \bar{\bar{\tau}}_q + \alpha_q \rho_q \vec{g} + \sum_{p=1}^{n}(\vec{R}_{pq} + \dot{m}_{pq}\vec{v}_{pq} - \dot{m}_{qp}\vec{v}_{qp}) + (\vec{F}_q + \vec{F}_{lift,q} + \vec{F}_{wl,q} + \vec{F}_{vm,q} + \vec{F}_{td,q})$$

The Eulerian-Eulerian model, apart from solving momentum and continuity equations for each phase, also shared a single pressure (∇p) between all phases. It is essential to recognize that this overall momentum balance could be streamlined according to specific phase interactions. Parameters such as the wall lubrication force for phase q ($\vec{F}_{wl,q}$), which are significant in scenarios like liquid-gas bubbly flows, become inconsequential for fluid-solid flows [14]. Additionally, between the general terms $\frac{\partial}{\partial t}\left(\alpha_q \rho_q\right)$ and $\nabla \cdot \left(\alpha_q \rho_q \vec{v}_q \vec{v}_q\right)$ that account for the time-varying and convective momentum transfer between the phases respectively, the time-varying term could be neglected due to the steady-state condition prescribed to all simulations in this study. These conditions lead to additional simplifications of the transport governing equations. To achieve a fluid-solid configuration, the general transport equation shown in Equation 2 was modified to represent the fluid-solid momentum equations used by ANSYS Fluent to solve for the solid and fluid phases respectively:

(3) $$\frac{\partial}{\partial t}(\alpha_s \rho_s \bar{v}_s) + \nabla \cdot (\alpha_s \rho_s \bar{v}_s \bar{v}_s) = -\alpha_s \nabla p - \nabla p_s + \nabla \cdot \bar{\bar{\tau}}_s + \alpha_s \rho_s \bar{g} + \sum_{l=1}^{N}(\bar{R}_{ls} + \dot{m}_{ls}\bar{v}_{ls} - \dot{m}_{sl}\bar{v}_{sl}) + \left(\bar{F}_s + \bar{F}_{lift,s} + \bar{F}_{vm,s} + \vec{F}_{td,s}\right)$$

(4) $$\frac{\partial}{\partial t}(\alpha_l \rho_l \bar{v}_l) + \nabla \cdot (\alpha_l \rho_l \bar{v}_l \bar{v}_l) = -\alpha_l \nabla p + \nabla \cdot \bar{\bar{\tau}}_l + \alpha_l \rho_l \bar{g} + \sum_{s=1}^{N}(\bar{R}_{sl} + \dot{m}_{sl}\bar{v}_{sl} - \dot{m}_{ls}\bar{v}_{ls}) + \left(\bar{F}_l + \bar{F}_{lift,l} + \bar{F}_{vm,l} + \vec{F}_{td,l}\right)$$

In the pneumatic two-phase flow studied, the subscripts s and l referred to the solid and fluid phases respectively. If more secondary phases were added to describe the polydisperse mixture, they could be accounted for in the general expressions shown by increasing the number of n^{th} phases solved for. Before utilizing the momentum equations shown using ANSYS Fluent solver, it was important to identify which terms would dominate the flow and which ones could be disregarded due to their negligible impact on the flow regime selected.

The virtual mass effect ($\bar{F}_{\mathrm{vm},q}$), an additional mass contribution attributed to a fluid particle when undergoing acceleration or deacceleration, was described as a force for phase q in Equation 2 and for the solid and fluid phase momentum equations in Equation 3 and Equation 4. The virtual mass force becomes significant usually when the secondary phase accelerates relative to the primary phase. In this case, in which the particle sizes studied remained below $500\mu m$ and their flows were mostly denoted by the fluid carrier phase, the particle phase was not found to undergo significant acceleration effects relative to the gaseous phase. Additionally, preliminary testing showed that the secondary phase did not experience substantial acceleration relative to the primary phase, further detailed in Appendix A.

Among the other parameters in the equation of motion, the turbulent dispersion force ($\vec{F}_{td,q}$), which represents the interphase turbulent momentum transfer and acts as a turbulent diffusion in dispersed flows, was neglected. Turbulent dispersion forces are mainly modeled to describe the spread of bubbles because of flow turbulence. In previous pneumatic conveying studies performed by Laín and Sommerfeld, it was found that turbulence dispersion forces were not very pronounced when particles exhibited

relatively low Reynolds Numbers [23]. The particle's Reynolds Numbers for the flows present in this study were found to be relatively small, implying that the turbulent dispersion force for this case would not be very significant. Further numerical validation for disregarding this term can be found in Appendix A.

In this scenario, where there were negligible virtual mass forces and turbulence dispersion forces acting on both continuous phases, both terms were disregarded. Additionally, the system analyzed did not experience any external forces ($\bar{F}_q$), allowing further simplification of the momentum equations. These simplifications aligned the general fluid-solid momentum equations with the specific configuration necessary to represent the solid-gas granular flow problem. In addition, the interphase forces between phases ($\bar{R}_{pq}$), referring to the forces acting between phases in the multiphase system due to friction, pressure, cohesion, and other effects [14], could further be expressed in terms of the velocities and fluid-solid exchange coefficients of the phases (K_{pq}), a parameter that characterized the rate at which mass, momentum and heat were transferred between the adjacent phases. For multiphase flows, this relationship was achieved by establishing symmetry between the interphase momentum exchange coefficient for both phases.

(5) $$\bar{\mathrm{R}}_{\mathrm{pq}} = \mathrm{K}_{\mathrm{pq}}\left(\bar{\mathrm{v}}_{\mathrm{p}} - \bar{\mathrm{v}}_{\mathrm{q}}\right) \qquad K_{pq} = K_{qp}$$

(6) $$\boldsymbol{\nabla} \cdot (\alpha_s \rho_s \bar{v}_s \bar{v}_s) = -\alpha_s \nabla p - \nabla p_s + \nabla \cdot \bar{\bar{\tau}}_s + \alpha_s \rho_s \bar{g} + \sum_{l=1}^{N} (K_{ls}(\bar{v}_l - \bar{v}_s) + \dot{m}_{ls}\bar{v}_{ls} - \dot{m}_{sl}\bar{v}_{sl}) + (\vec{F}_{lift,s})$$

(7) $$\boldsymbol{\nabla} \cdot (\alpha_l \rho_l \bar{v}_l \bar{v}_l) = -\alpha_l \nabla p + \nabla \cdot \bar{\bar{\tau}}_l + \alpha_l \rho_l \bar{g} + \sum_{s=1}^{N} (K_{sl}(\bar{v}_s - \bar{v}_l) + \dot{m}_{sl}\bar{v}_{sl} - \dot{m}_{ls}\bar{v}_{ls}) + (\bar{F}_{lift,l})$$

B. Granular Property Models

The interphase exchange coefficient is formulated as a function of the particle's drag coefficient (C_D) and particle Reynolds number (Re_s). This allows for the selection of a drag coefficient model that suits the characteristics of the established granular case. Specifically, Wen and Yu introduced a fluid-solid exchange coefficient suitable for dilute flows [24]:

(8) $$\mathrm{K_{ls}} = \frac{3}{4}\frac{\alpha_s\alpha_l\rho_l|\vec{v}_s-\vec{v}_l|}{d_s}\mathrm{C_D}\alpha_l^{-2.65}$$

(9) $$\mathrm{C_D} = \frac{24}{\alpha_l \mathrm{Re_s}}[1 + 0.15(\alpha_l \mathrm{Re_s})^{0.687}]$$

(10) $$\mathrm{Re_s} = \frac{\rho_l d_s|\vec{v}_s-\vec{v}_l|}{\mu_l}$$

The particle's relative Reynold's Number, representing the ratio of inertial forces to viscous forces exerted from the fluid phase to the solid phase, was necessary for determining the drag effects experienced by the particulate phase [25]. When examining the momentum equations for the solid and fluid phases presented in Equation 6 and Equation 7, the lift force ($\vec{F}_{lift}$), which accounted for the forces acting on the solid particles suspended by the gaseous phase, remained a critical consideration. In the

discussion of the lift forces experienced by the particles, the general expression for the lift force was defined as [14]:

$$\vec{F}_{lift} = -C_l \rho_s \alpha_l (\vec{v}_s - \vec{v}_l) \times (\nabla \times \vec{v}_s) \tag{11}$$

From the available models provided by ANSYS Fluent, the Saffman-Mei model proved to be a suitable choice for simulating the lift drag coefficient experienced by the granular phase, particularly under the assumption that the particles were spherical solids [26]. Mei and Klausner extended this model to be applicable to a wider range of particle Reynolds' Numbers, thereby enhancing its versatility in multiple applications [27]. In addition to Mei and Klausner enhancing the model, Laín evaluated the model's adequacy in describing particle behavior by including it in his Eulerian-Lagrangian model and successfully validating it with experimental data [6].

The model calculates the lift coefficient (C_l) for a range of particle Reynold's numbers using the aerodynamic lift resulting from the interaction between both phases and the vorticity-induced lift resulting from interaction between particles and vortices shed by particle wakes [14]. To express the vorticity effects, the Reynolds number based on particle vorticity (Re_ω) was calculated. A dimensionless parameter (β) was defined to compare the vorticity and particle size effects on the flow and determine what parameters determined the flow behavior. The lift coefficient could then be expressed as a function of both Reynold's numbers, and β:

$$C_i = \frac{3}{2\pi\sqrt{Re_w}} C'_l \qquad C'_l = \begin{cases} 6.46 \times f(Re_s, Re_\omega) & Re_p \leq 40 \\ 6.46 \times 0.0524(\beta Re_p)^{\frac{1}{2}} & 40 < Re_p < 100 \end{cases} \tag{12}$$

(13) $$\beta = 0.5\left(\frac{Re_\omega}{Re_p}\right) \qquad f(Re_s, Re_\omega) = (1 - 0.3314\beta^{0.5})e^{-0.1Re_p} + 0.3314\beta^{0.5}$$

(14) $$Re_\omega = \frac{\rho_s|\nabla\times\vec{v}_s|d_s^2}{\mu_s}$$

Similar to the lift force, addressing the solids pressure term within the momentum equation is crucial for accurately representing the system. The solids pressure (p_s), referring to the pressure exerted by the solid particles in the multiphase flow system, can be defined for dilute flows consisting of a single solid phase by using the expression shown in Equation 15:

(15) $$p_s = \alpha_s\rho_s\theta_s + 2\rho_s(1 + e_{ss})\alpha_s^2 g_{0,ss}\Theta_s$$

It was possible to extend Equation 15 for scenarios where multiple solid phases needed to be used to describe particle size differences within the polydisperse mixture studied. The following general solids pressure formulation in the presence of multiple solid phases, derived by Gidaspow [16], were applied by the solver to describe each PSD studied:

(16) $$p_{s_1} = \alpha_{s_1}\rho_{s_1}\theta_{s_1} + \left(\sum_{p=1}^{N}\frac{d_{s_2s_1}^3}{d_{s_1}^3}\left[2\left(1 + e_{s_2s_1}\right)g_{0,s_2s_1}\alpha_{s_1}\alpha_{s_2}\right]\right)\rho_{s_1}\Theta_{s_1}$$

(17) $$d_{s_2 s_1} = \frac{d_{s_2} + d_{s_1}}{2}$$

Via these models, the solids pressure was able to represent how the solid particles contributed to the overall pressure field in the system. Given that solids pressure is influenced by a radial distribution function (g_0), which acts as a correction factor adjusting the probability of collisions between particles, it was crucial to choose a radial distribution function model that aligned with the selected solids pressure model. In compacted flows, where there is a larger number of particle-particle interactions, the radial distribution function exhibits a major influence on the granular properties [14]. However, in the chosen dilute flow regime the radial distribution function becomes less significant as the probability of particle collisions decreases. For this problem configuration, the radial distribution function model has been selected to agree with Lun et al and Gidaspow derivations, due to its applicability in characterizing dilute flows [28].

The values of the radial distribution function depended on the maximum packing limit of the mixture ($\alpha_{s,max}$). The maximum packing limit refers to the maximum solid volume fraction achievable in a granular assembly when particles are arranged in a manner that allows for the densest packing. For this study, the maximum packing limit was set to a constant value of 0.63. This choice was motivated by the diluted nature of the solid-gas flow mixture, alleviating concerns about reaching the established maximum packing limit value. The general expressions for the radial distribution function model selected, applicable in the presence of a single solids phase and multiple solid phases, are shown in Equation 18 and Equation 19:

(18) $$g_0 = \left[1 - \left(\frac{\alpha_s}{\alpha_{s,max}}\right)^{\frac{1}{3}}\right]^{-1}$$

(19) $$g_{0,ll} = \left[1 - \left(\frac{\alpha_s}{\alpha_{s,max}}\right)^{\frac{1}{3}}\right]^{-1} + \frac{1}{2} d_l \sum_{k=1}^{N} \frac{\alpha_k}{d_k} \qquad \alpha_s = \sum_{k=1}^{N} \alpha_k$$

Within the Eulerian-Eulerian model, the Kinetic Theory of Granular Flows (KTGF) incorporated the stress-strain tensor ($\bar{\bar{\tau}}$) to account for shear and bulk viscous effects experienced by both phases. The stress-strain tensor for the solid phase ($\bar{\bar{\tau}}_s$), shown in the fluid-solid momentum expression described in Equation 6, could be expressed in terms of the solid phase properties. The stress-strain tensor for the solid phase is described below in Equation 20:

(20) $$\bar{\bar{\tau}}_s = \alpha_s \mu_s (\nabla \vec{v}_s + \nabla \vec{v}_s^T) + \alpha_s \left(\lambda_s - \frac{2}{3}\mu_s\right) \nabla \cdot \vec{v}_s \bar{\bar{I}}$$

The stress-strain tensor can also be expressed for the fluid phase l to solve for the gaseous phase transport expression shown in Equation 7. The solids stress-strain tensor represents the average stress distribution within the solid phase, measuring the internal forces acting on the particles due to external loads and deformation influenced by the gaseous phase.

Within the solids stress-strain tensor expression, the solids bulk viscosity (λ_s), a parameter that reflects the resistance of granular particles to compression and expansion [14], was defined to be zero for the established problem configuration. In this system, the

glass beads were anticipated to remain mostly rigid and non-deformable due to the dilute flow regime in which they operated, further limiting the possibility of interaction between particles. These assumptions neglected the bulk viscosity's influence prevalent in Equation 20. This justification can further be validated using Lun et. al's bulk viscosity model [28], in which for dilute flows with low solids volume fraction (α_s), the bulk viscosity tends to zero:

$$\lambda_s = \frac{4}{3}\alpha_s^2 \rho_s d_s g_{0,ss}(1 + e_{ss})\left(\frac{\Theta_s}{\pi}\right)^{\frac{1}{2}} \tag{21}$$

Apart from bulk viscosities, the solids stress tensor also describes the effects of shear stresses on the particles via a solids shear viscosity term (μ_s). In this way, the stress-strain tensor can encompass shear and bulk viscosities resulting from particle momentum exchange attributed to translation, collision, and friction [14]. The solids shear viscosity is defined as:

$$\mu_s = \mu_{s,col} + \mu_{s,kin} + \mu_{s,fr} \tag{22}$$

The collisional viscosity term ($\mu_{s,col}$) refers to the resistance to flow exhibited by the solid particles due to frequent inter-particle collisions within the fluid. It arises from the momentum exchange during collisions among the particles and affects the overall behavior of the solid phase within the multiphase flow. The collisional viscosity can be expressed in the following form [15]:

(23) $$\mu_{s,col} = \frac{4}{5}\alpha_s \rho_s d_s g_{0,ss}(1+e_{ss})\left(\frac{\Theta_s}{\pi}\right)^{\frac{1}{2}}$$

For the kinetic viscosity term ($\mu_{s,kin}$), which refers to the resistance of individual particles to deformation as they move through the fluid phase, the Gidaspow model was chosen to uphold consistency with the models utilized to describe previous flow parameters [15]. The radial distribution function was also employed in the calculation of this parameter, emphasizing the significance of maintaining consistency within the chosen models:

(24) $$\mu_{s,kin} = \frac{10\rho_s d_s\sqrt{\Theta_s \pi}}{96\alpha_s(1+e_{ss})g_{0,ss}}\left[1+\frac{4}{5}g_{0,ss}\alpha_s(1+e_{ss})\right]^2$$

The frictional viscosity term ($\mu_{s,fr}$) shown in Equation 24 describes the additional resistance to flow experienced by the solid particles when particle interlocking, and entanglement occurs at maximum packing limits. Moreover, the influence of the frictional viscosity term was identified to be negligible in this study due to the dilute nature of the system, resulting in minimal frictional interactions between particles. Both bulk and frictional viscosity terms are more prevalent in dense systems, which do not align with the targeted flow regime of this study. Thus, the resulting shear viscosity term simplified to the following:

(25) $$\mu_s = \mu_{s,col} + \mu_{s,kin}$$

Both shear viscosity and solids pressure models are calculated using the granular temperature of the solid phase (θ_s). Granular temperature, which functions as a measure of the thermal and kinetic energies associated with the random movement of particles within the granular system, was expressed as a partial differential equation (PDE). The PDE transport equation derived from Kinetic Theory of Granular Flows (KTGF) is represented below as the following [17]:

$$\frac{3}{2}\left[\frac{\partial}{\partial t}(\rho_s\alpha_s\theta_s) + \nabla\cdot(\rho_s\alpha_s\vec{v}_s\theta_s)\right] = \left(-p_s\bar{\bar{I}} + \bar{\bar{\tau}}_s\right):\nabla\vec{v}_s + \nabla\cdot\left(k_{\theta_s}\nabla\theta_s\right) - \gamma_{\theta_s} + \varphi_{ls} \quad (26)$$

To solve the granular temperature PDE, it is required to select a granular conductivity model (k_{θ_s}) in the system to find the granular energy diffusive flux ($k_{\theta_s}\nabla\theta_s$). The granular conductivity can be represented using the Gidaspow model [15] as the following:

$$k_{\theta_s} = \frac{150\rho_s d_s\sqrt{\theta\pi}}{384(1+e_{ss})g_{0,ss}}\left[1+\frac{6}{5}\alpha_s g_{0,ss}(1+e_{ss})\right]^2 + 2\rho_s\alpha_s^2 d_s(1+e_{ss})g_{0,ss}\sqrt{\frac{\Theta_s}{\pi}} \quad (27)$$

The granular temperature PDE also utilizes a collisional dissipation of energy model derived by Lun et al. [28] to represent the rate of energy dissipation within the solids phases due to collision between particles:

(28) $$\gamma_{\Theta m} = \frac{12(1-e_{ss}^2)g_{0,ss}}{d_s\sqrt{\pi}}\rho_s\alpha_s^2\Theta_s^{\frac{3}{2}}$$

The transfer of the kinetic energy from random fluctuations in the particle velocity from the solids phase to the fluid phase (φ_{ls}), another term utilized in the formulation of the granular temperature PDE, was represented following the expression derived by Gidaspow [15]:

(29) $$\varphi_{ls} = -3K_{ls}\Theta_s$$

After concluding the numerical approach analysis for the fluid-solid momentum transfer equations and phase property models for each phase, it was important to identify the numerical techniques used to define the system's boundary conditions.

C. Wall Boundary Conditions and Turbulence Modeling

To fully represent the granular phases, it was essential to include wall boundary conditions to address the wall shear forces and granular temperature effects at the walls of the simulated pneumatic conveyor. These wall conditions were contingent on the specularity coefficient (ϕ), the coefficient of restitution between the particle and the walls to describe particle-wall interactions (e_{sw}), and the particle slip velocities parallel to the wall ($\vec{U}_{s,|}$). For this boundary, the specularity coefficient determined the fraction of collisions that would transfer momentum to the wall. The specularity coefficient ranged from 0 to 1, with 0 representing perfect specular collisions and 1 representing perfectly diffuse collisions, such as those obtained from the no-slip boundary condition [34]. The coefficient of restitution, which represented the amount of kinetic energy retained or lost by each particle when colliding, was set to 0.9, mirroring Laín's study [6], and the specularity coefficient was set to 0.1. The expressions governing the shear forces at the wall ($\vec{\tau}_s$) and granular temperatures at the wall in the modeling simulation were:

(30) $$\vec{\tau}_s = -\frac{\pi}{6}\sqrt{3}\phi\frac{\alpha_s}{\alpha_{s,max}}\rho_s g_0\sqrt{\Theta_s}\vec{U}_{s,|}$$

(31) $$q_s = \frac{\pi}{6}\sqrt{3}\phi\frac{\alpha_s}{\alpha_{s,max}}\rho_s g_0\sqrt{\Theta_s}\vec{U}_{s,|}\cdot\vec{U}_{s,|} - \frac{\pi}{4}\sqrt{3}\frac{\alpha_s}{\alpha_{s,max}}(1-e_{sw}^2)\rho_s g_0\Theta_s^{\frac{3}{2}}$$

The heat flux (q_s) in Equation 31 was able to describe the energy transferred between the granular phase and the wall using the Johnson and Jackson model [29]. For

turbulence modeling in the simulated pneumatic conveyor, a new set of transport equations was established to account for turbulent fluctuation effects. Among the turbulence models, the RNG k−ε model, also known as the renormalization grouping dispersed turbulent kinetic energy and dissipation rate model, was selected. Tai and Chi-Hwa evaluated the model and portrayed it to be ideal for systems with dilute concentrations of the secondary phases [30]. It is particularly well-suited when using a two-way coupling scheme, making it optimal for this problem configuration.

The RNG k−ε model, similar in form to the standard k−ε model, differs from it by including an additional term in its dissipation rate equation, providing more accurate results for a wider range of flows [14]. The RNG k−ε turbulent model's transport equations were as following:

(32) $$\frac{\partial}{\partial t}(\rho k) + \frac{\partial}{\partial x_i}(\rho k u_i) = \frac{\partial}{\partial x_j}\left(\alpha_k \mu_{eff} \frac{\partial k}{\partial x_j}\right) + G_k + G_b - \rho\varepsilon - Y_M + S_k$$

(33) $$\frac{\partial}{\partial t}(\rho\varepsilon) + \frac{\partial}{\partial x_i}(\rho\varepsilon u_i) = \frac{\partial}{\partial x_j}\left(\alpha_\varepsilon \mu_{eff} \frac{\partial \varepsilon}{\partial x_j}\right) + C_{1\varepsilon}\frac{\varepsilon}{k}(G_k + C_{3\varepsilon}G_b) - C_{2\varepsilon}\rho\frac{\varepsilon^2}{k} - R_\varepsilon + S_\varepsilon$$

D. Population Balance Model

In addition to turbulence modeling, particle size distributions need to be incorporated within the Eulerian-Eulerian model to accurately depict the polydisperse mixture. To model the particle-size-dependent dynamics within the simulated pneumatic conveyor, an inhomogeneous discrete population balance model was employed. This modeling approach facilitated the representation of each particle size distribution by dividing them into distinct bins, each representing a finite range of particle sizes. By considering each bin as an independent phase, the fluid-solid momentum equations could be solved separately for each phase, enabling a detailed analysis of particle flow behaviors based on their size distributions. This method captured variations in velocity gradients and particle concentration patterns, providing a better understanding of how particles within this polydisperse system behaved. The transport equation for the discrete bin fraction (f_i) could be represented as the following:

$$\frac{\partial}{\partial t}(\rho \alpha f_i) + \nabla \cdot \left(\vec{u}_p \alpha f_i\right) = S_{bi} \tag{34}$$

The bin fraction represented the total number of particles that would fall within a defined bin or particle size range. Since the solid phase consisted of a mixture of differently sized particles, the total solids volume fraction of the mixture could be represented into segments characterizing specific particle size ranges. Each bin corresponded to a particle size range, consisting of a portion of the total solid's volume

fraction available in the system. In Equation 34, the net mass source for particles (S_{bi}) described the net effect that breakage and agglomeration of particles could have on the established bins. If particles increased or decreased in size due to any of these processes, leading to the particles no longer belonging to their initial prescribed bin, this source term could be changed to account for these changes and adjust the new particle size distribution accordingly. For the inhomogeneous discrete method, in which bins with different particle size ranges were assigned to multiple solid phases to allow advection by different phase velocities [14], the net mass source for a given phase was expressed as:

$$S_i = \sum_{i=1}^{M} S_{bi} \tag{35}$$

As mentioned previously, bins in the inhomogeneous model for a phase can migrate to another phase through breakage or agglomeration, creating a net mass source term for phases present. However, this was not the case for the solid particles used in this study. The glass bead particles present in this study were assumed to not experience these phenomena due to the particle characteristics specified for them, which would not lead to any adhesion or breakage of the particles. With all these models accounting for phase properties, wall boundaries, turbulence and particle size distributions, the Eulerian-Eulerian framework could be introduced to fully encapsulate the fluid dynamics of the granular flow.

III. METHODOLOGY

A. Overview of Proposed Eulerian-Eulerian Model

The proposed Eulerian-Eulerian model was developed to investigate crucial parameters essential for designing pneumatic dilute-phase conveying systems, focusing on pressure drop profiles, velocity gradients, and particle concentrations for each phase. In this study, where the key parameters depended primarily on the momentum transfer effects between phases, the system was configured to operate under room conditions to facilitate the selection of the computational models implemented within the Eulerian-Eulerian framework. By assigning constant room temperature and density values to the geometry and all phases involved, the energy equations for each phase could be omitted due to the minimal heat transfer effects caused by the absence of heat sources and insubstantial temperature gradients in the system.

To implement the Eulerian-Eulerian model and create the simulated pneumatic conveying system, ANSYS Fluent, the referenced CFD tool used to simulate fluid flow, was introduced. The modeled geometry in this study imitated Laín and Sommerfeld's dimensions, phase descriptions and boundary conditions used for their Eulerian-Lagrangian simulation [6]. The problem configuration replicated a two-phase polydisperse flow consisting of air and glass bead particles, both initially moving at $27\,\frac{\mathrm{m}}{\mathrm{s}}$ through a 150 mm diameter, 10.6 m long pipe. A visual representation of the geometry with its boundary conditions is shown in Figure 1 and a more detailed preview of the geometry, material properties, and boundary conditions used in this study are shown in Table 1, 2 and 3 below:

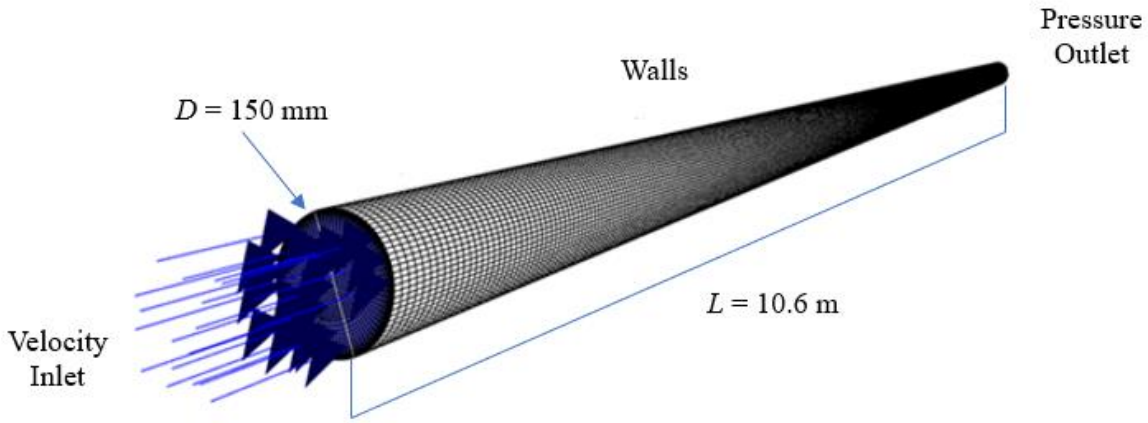

Figure 1: Horizontal Pipe Geometry with Boundary Conditions

Table 1: Dimensions for Horizontal Pneumatic Conveying Pipe

Geometry	Length [m]	Diameter [mm]
Circular Pipe	10.6	150

Table 2: Property Values for Primary and Secondary Phases

Phase	Phase Type	Material	Density $\left[\frac{kg}{m^3}\right]$	Viscosity $\left[\frac{kg}{m \cdot s}\right]$
Primary Phase	Fluid	Air	1.225	1.7894e-05
Secondary Phase	Solid (Pseudo-fluid)	Glass-Beads	2500	

Table 3: Boundary Conditions for Gaseous and Solid Phases

Phase	Inlet Velocity $\left[\frac{m}{s}\right]$	Inlet Volume Fraction	Coefficient of Restitution	Specularity Coefficient	Granular Temperature $\left[\frac{m^2}{s^2}\right]$	Wall Roughness $[\mu m]$
Air	27	0.999657	N/A	N/A	N/A	50
Glass-Beads	27	0.000343	0.9	0.1	0.0001	50

To further validate the granular property models selected, a sensitivity study was conducted to investigate particle velocity and volume fraction solution variability when using different granular models. Variability between the Syamlal-Obrien and Gidaspow models was investigated for granular viscosity and granular temperature PDE models. For drag coefficient models, cases using the Syamlal-Obrien, Gidaspow and Wen-Yu models were analyzed. Solids pressure and radial distribution functions for Syamlal-Obrien and Lun et. al were studied, as well as the model's sensitivity for different granular inlet temperatures ranging from $0.0001\,\frac{\mathrm{m}^2}{\mathrm{s}^2}$ to $0.1\,\frac{\mathrm{m}^2}{\mathrm{s}^2}$ was investigated. ANSYS Fluent's pressure-based solver and all granular properties selected based on previous works and preliminary sensitivity studies were used consistently to solve all simulations in this report. A more detailed review of the preliminary sensitivity test results obtained for each granular model can be found in Appendix B. A summary of the final simulation settings selected based on all sensitivity studies performed and on literature are shown:

Table 4: Eulerian-Eulerian Model Simulation Settings

Multiphase Model	Solving Scheme	Solver type
Eulerian Model	Implicit	Pressure-based Solver
Solids Pressure	Radial Distribution Function	Granular Temperature PDE
Lun et. al	Lun et. al	Gidaspow
Granular Conductivity	Granular Viscosity	Granular Inlet Temperature $\left[\frac{m^2}{s^2}\right]$
Gidaspow	Gidaspow	0.0001
Drag coefficient	Lift coefficient	Turbulent Model
Wen-Yu	Saffman−Mei	RNG-k-ε
Wall-Boundary	Population Balance Model	
Johnson−Jackson	Inhomogeneous Discrete Method	

Using these settings, flow solution data was gathered for all cases from two regions of interest within the horizontal pipe. The first region of interest was the pipe's centerline, in which pressure drop data was extracted from a horizontal line passing directly through the center of the pipe to obtain an overview of the overall pressure drop in the system. For particle velocity profiles and volume fraction distributions, data was extracted from a vertical line in the y-axis, drawn 8 m away from the pipe's inlet. These locations coincide with regions where Laín and Sommerfeld reported data to validate the simulated model against experimental results. These regions of interest are highlighted in Figure 2.

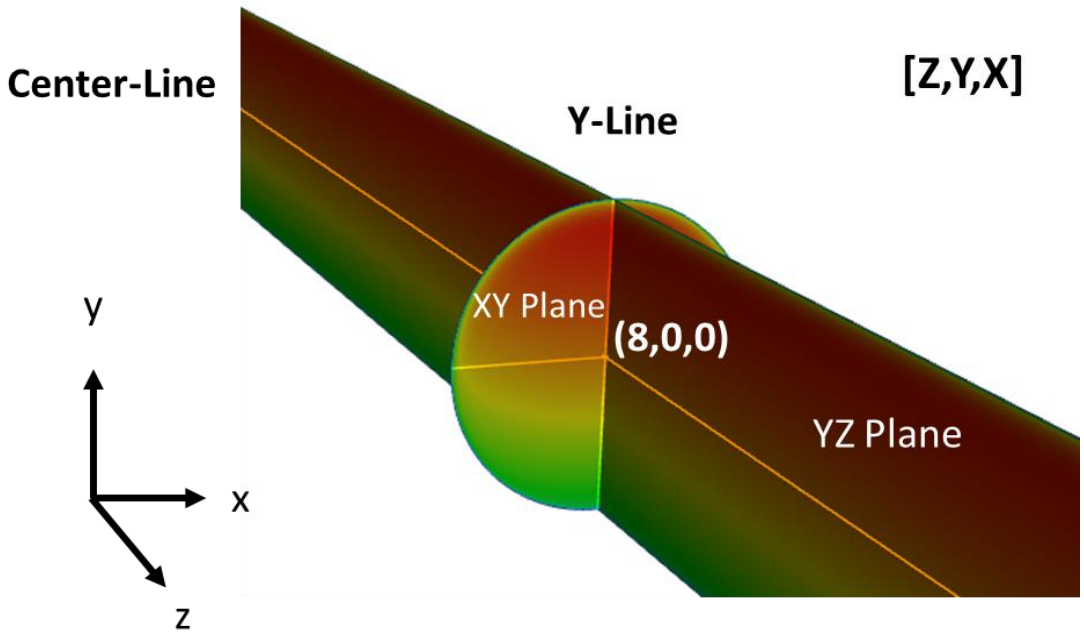

Figure 2: Regions of Interest for Property Data Extraction

B. Laín and Sommerfeld Comparative Study

To fully capture the polydisperse nature of the solid-fluid flow from Laín and Sommerfeld's study and validate the proposed model, an inhomogeneous discrete population balance approach was selected. After discretizing Laín's PSD data, it was found that a small portion of the mixture consisted of a minimum particle size of approximately 1.7 μm and a maximum of approximately 99 μm, establishing the minimum and maximum particle size ranges that could be observed in the mixture. Using the data extracted from the PSD, simulations representing the polydisperse mixture as a series of bins were performed. The tools used to digitalize Laín's data and to calculate the bin fractions for each particle size group were Automeris [31], and a specialized PSD calculator available from the Combustible Dust Performance-Based Design Center [32], respectively.

After proving in Chapter IV that the solutions converged independently of mesh size used, a series of simulations were performed to compare Laín's experimental results and validate the Eulerian-Eulerian framework selected. The first case consisted of simulating the particulate phase as a monodisperse mixture. The monodisperse case was made of particles with a diameter of 40 μm, which was the number mean diameter reported by Laín and Sommerfeld from their PSD. The rest of the cases consisted of simulating Laín's PSD via the inhomogeneous discrete population balance model by using a series of bins to characterize the mixture. Cases consisting of two, five, ten, twenty and thirty bins were investigated. Bin convergence was studied for these cases to determine the number of bins needed for the solution to achieve significant agreement

with the case employing the highest number of bins. From these analyses, agreement between both monodisperse and polydisperse simulations could be established when compared to Laín's experimental results. Laín and Sommerfeld's particle size distribution discretized into the five different bin configurations mentioned can be seen in Figures 3-7.

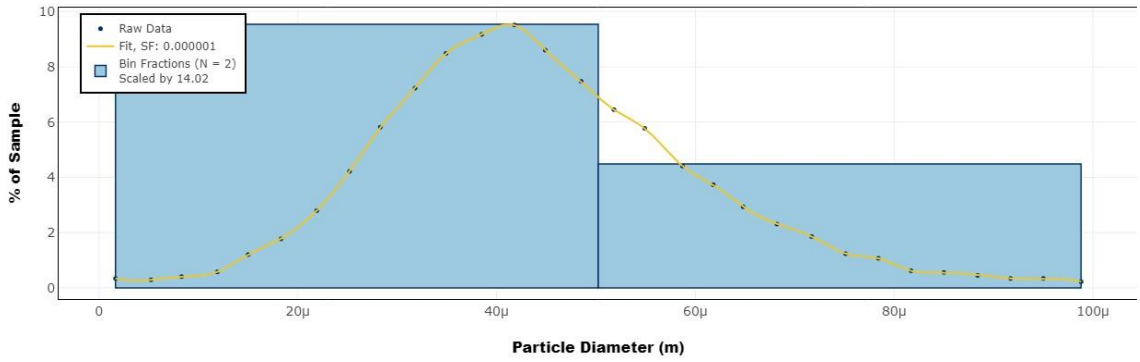

Figure 3: Laín and Sommerfeld's PSD Discretized into 2 Bins

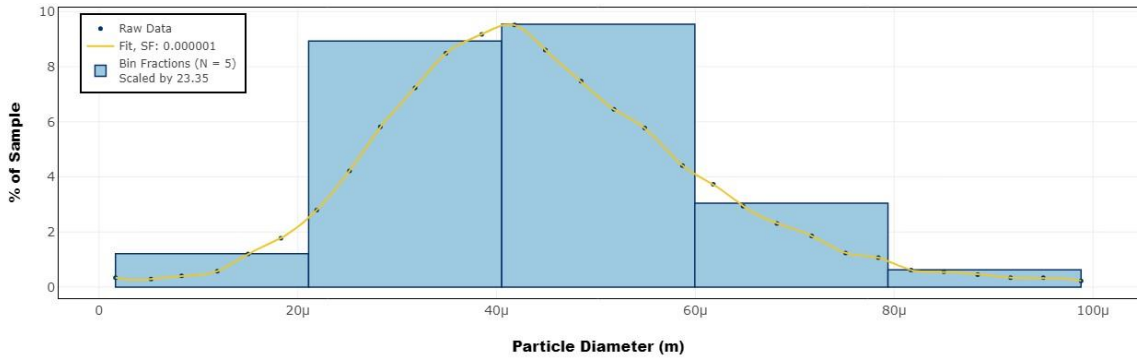

Figure 4: Laín and Sommerfeld's PSD Discretized into 5 Bins

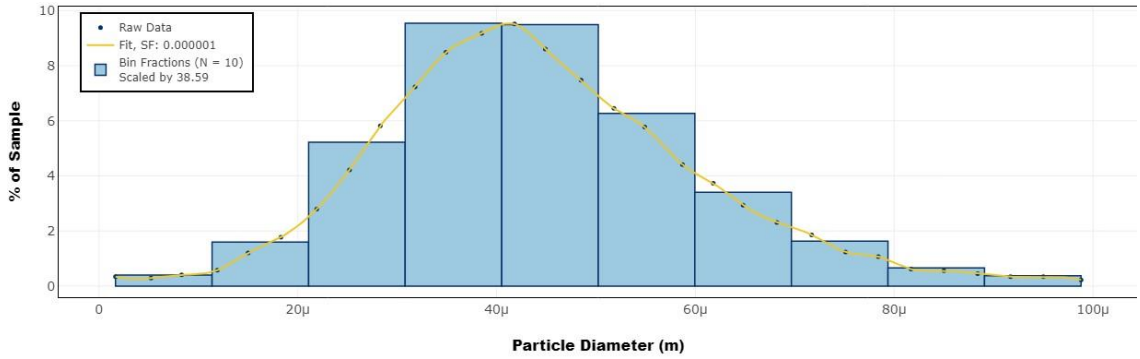

Figure 5: Laín and Sommerfeld's PSD Discretized into 10 Bins

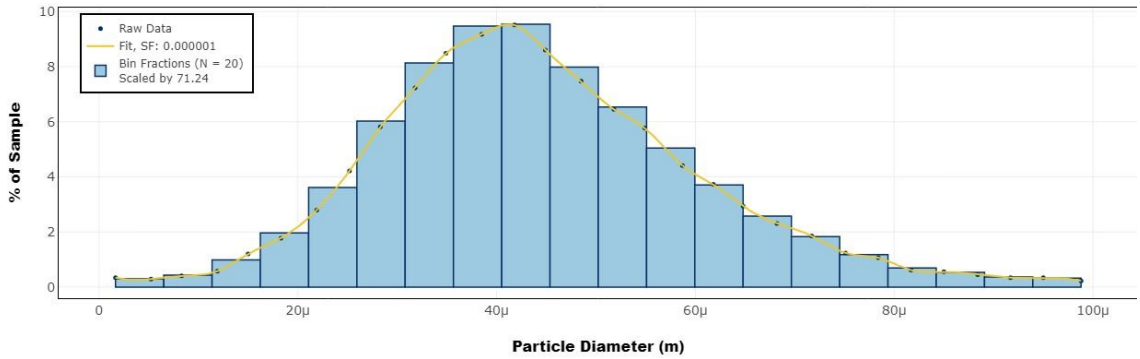

Figure 6: Laín and Sommerfeld's PSD Discretized into 20 Bins

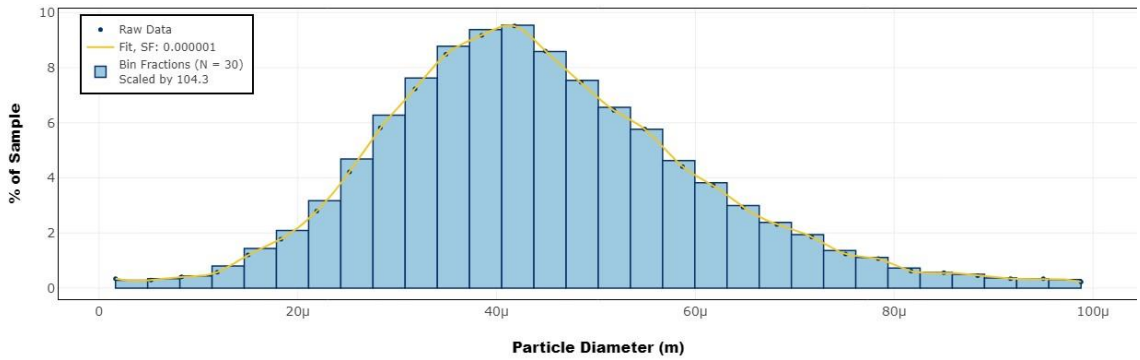

Figure 7: Laín and Sommerfeld's PSD Discretized into 30 Bins

C. Particle Size Distribution Variance Study

After analyzing the mean diameter monodisperse case and the polydisperse bin cases using Laín's PSD alongside experimental data, a new study was conducted involving four additional particle size distributions ranging from 5 μm to 500 μm. This study explored the number of bins necessary for pressure drop solutions to converge and examined alternative methods that could be implemented to represent the polydisperse mixture as a simpler monodisperse case. Each PSD was formulated differently from each other by shifting the overall mean of the particle distribution. Three of the four PSD established were single peak distributions, while the fourth one was a three-peak distribution. The mean values for the particle size distributions studied were 250 μm, 325 μm, and 175 μm for the first three single-peak distributions respectively, and 250 μm for the fourth three-peak distribution. By evaluating three single peak cases with different overall distribution mean, it was possible to investigate if variations in particle sizes within the distribution significantly affected the overall pressure drop of the system. The fourth case aimed to determine whether variations in particle distribution shape significantly influenced solution accuracy when employing different particle size characterization techniques. The particle size distributions studied are shown below in Figures 8-11 and Table 5:

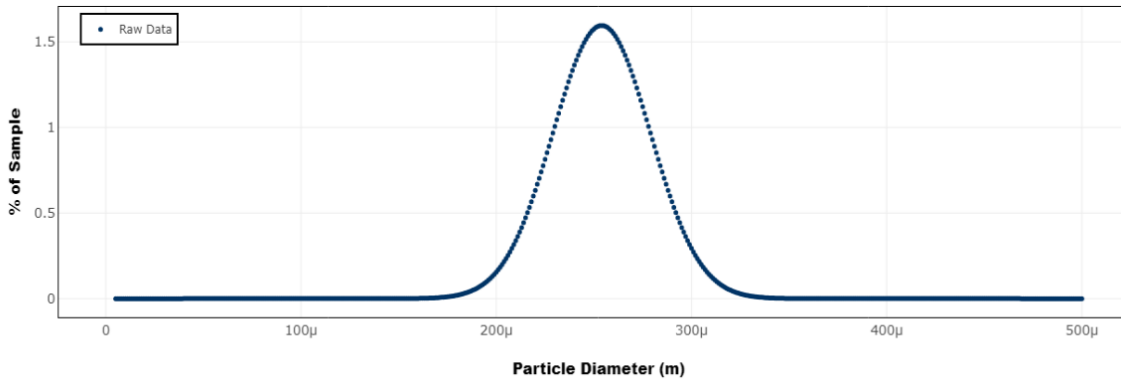

Figure 8: Particle Size Distribution #1

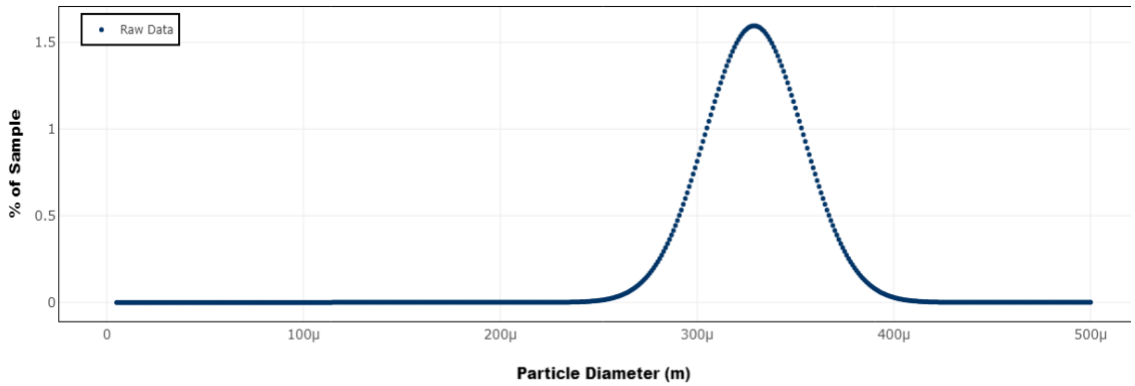

Figure 9: Particle Size Distribution #2

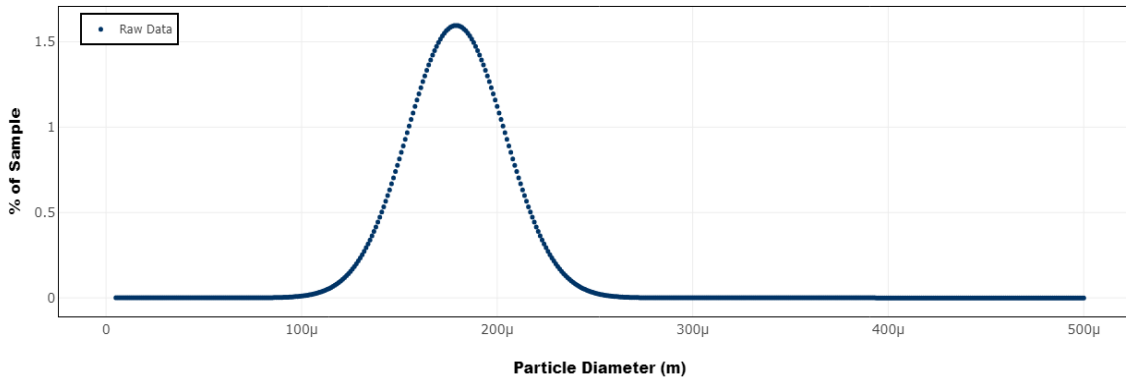

Figure 10: Particle Size Distribution #3

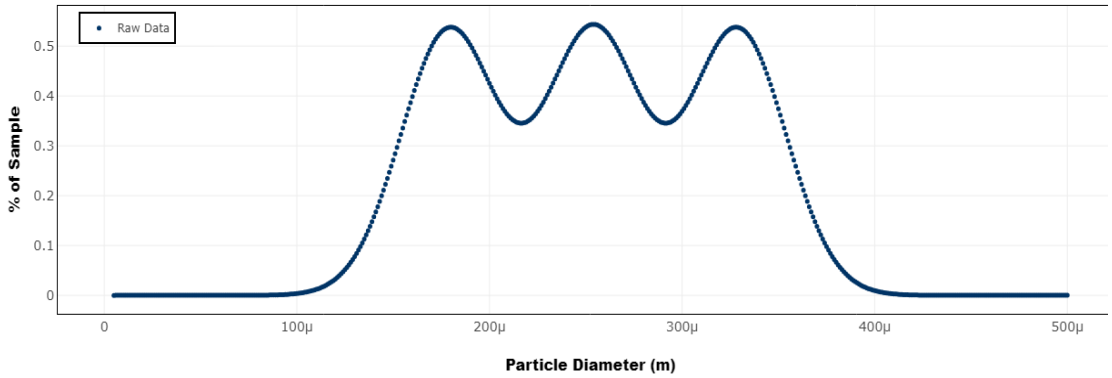

Figure 11: Particle Size Distribution #4

Table 5: Characteristics of Particle Size Distributions

Particle Size Distribution	Mean, μ (μm)	Standard Deviation, σ (μm)
PSD-#1	250	25
PSD-#2	325	25
PSD-#3	175	25
PSD-#4	250	25

D. Independent Mesh Convergence Study

To ensure solution stability, a mesh convergence analysis was performed following Laín's meshing techniques. This analysis provided crucial insights into the convergence behavior of the model, ensuring the reliability and accuracy of the simulation results obtained for the studied flow parameters. The mesh was divided into three main edge sizing techniques, each describing a region with a different number of divisions needed to replicate Laín and Sommerfeld's grid. This method gave rise to a reliable meshing structure that could produce results comparable with Laín's experimental data. The meshing framework and defined regions are shown in Figure 12 and Figure 13:

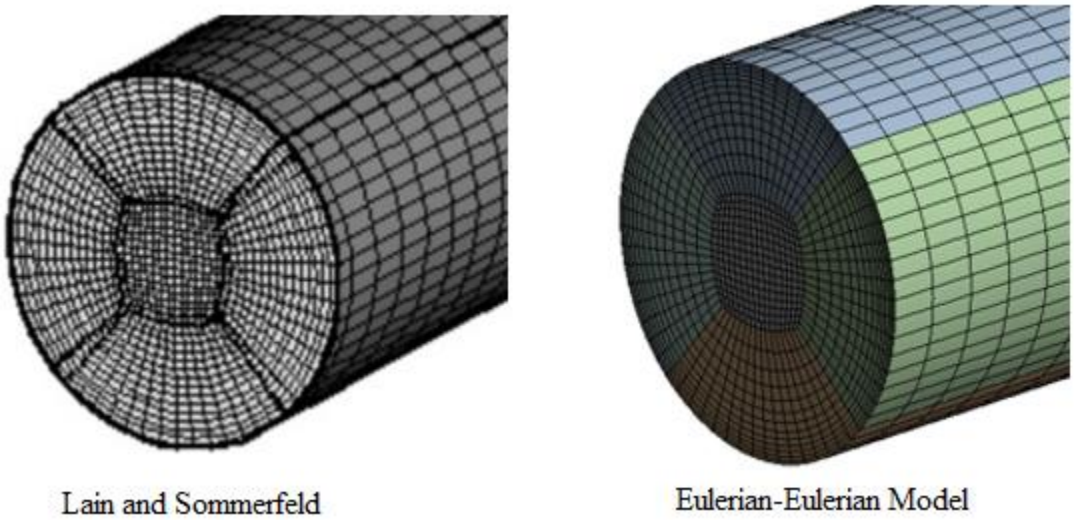

Figure 12: Grid Framework for Laín's Study and Proposed Model

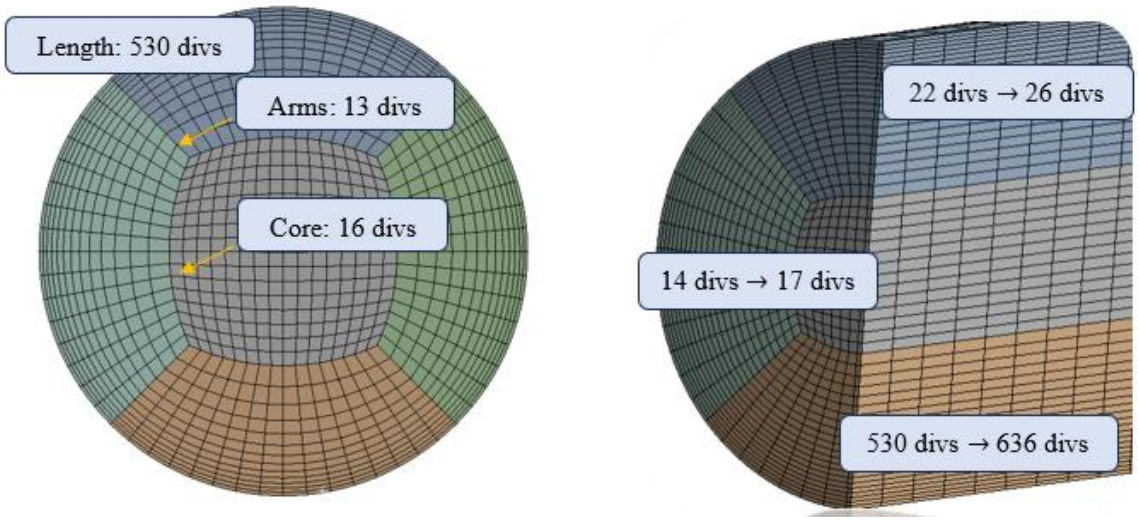

Figure 13: Grid Edge Sizing Structure for Proposed Model

Following the mesh structure shown in Figure 13, a mesh convergence study was conducted using five grid variations, each one characterized by a different number of elements. The five grid variations utilized the three main regions described in Figure 13 to increase the number of divisions present in the mesh, hence refining the mesh, improving its quality and bettering solution convergence. The specific configurations used to create the five derived grid variations are shown in Table 6:

Table 6: Grid Variations for Mesh Convergence Cases

Mesh Name	Nodes	Elements	Length Divisions	Arms Division	Core Divisions
MCS-#1	1,278,320	310,050	450	10	13
MCS-#2	2,361,829	576,640	530	13	16
MCS-#3	3,538,008	867,350	550	16	19
MCS-#4	4,452,344	1,093,680	560	18	21
MCS-#5	4,611,144	1,132,740	565	19	22

Using the mesh sizes provided in Table 6, two mesh convergence studies were conducted. One study aimed to prove that pressure drop, particle velocity and volume fraction solutions converged independently of the grid selected using the minimum particle diameter size available in Laín and Sommerfeld's PSD. The second study addressed convergence for these same parameters using the maximum available particle size. The main goal of these two studies was to implicitly prove that by reaching grid convergence using the minimum and maximum particle sizes within the PSD, any solutions obtained for the rest of the particle diameters within the distribution would be grid independent as well. The ten cases conducted using the minimum and maximum particle sizes available in Laín and Sommerfeld's PSD have been described in Table 7.

Table 7: Mesh Convergence Study for Laín's PSD

Minimum Particle Diameter Cases	Mesh	Particle Diameter [μm]
MCS-Min-#1	MCS-#1	1.66
MCS-Min-#2	MCS-#2	1.66
MCS-Min-#3	MCS-#3	1.66
MCS-Min-#4	MCS-#4	1.66
MCS-Min-#5	MCS-#5	1.66
Maximum Particle Diameter Cases	**Mesh**	**Particle Diameter [μm]**
MCS-Max-#1	MCS-#1	98.88
MCS-Max-#2	MCS-#2	98.88
MCS-Max-#3	MCS-#3	98.88
MCS-Max-#4	MCS-#4	98.88
MCS-Max-#5	MCS-#5	98.88

After completing the two mesh convergence studies for pressure drop, particle velocity and volume fraction distributions, grid MCS-#4 was selected to run a comparative analysis of the Eulerian-Eulerian model established with respect to Laín and Sommerfeld's experimental data. By doing so, the effectiveness of the model to predict accurate data could be validated.

In addition to the previous mesh convergence study, an additional grid independence study was conducted to analyze pressure drop data for the four newly generated particle size distributions. The new particle size distributions consisted of particles with diameter sizes between 5 µm to 500 µm. Since a newly established maximum particle size range of 500 µm was used for the four PSD, which bypassed the previous PSD range proposed by Laín and Sommerfeld, a new mesh convergence study was required to validate the grid selected for describing the particle sizes that would fall within the new range. Therefore, a new mesh convergence study was conducted to investigate pressure drop convergence for the new maximum particle size limit of 500 µm. This study utilized the same five grid variations as before, as shown in Table 8:

Table 8: Mesh Convergence Study for New PSDs

Maximum Particle Diameter New Case	Mesh	Particle Diameter [µm]
MCS-500μm-#1	MCS-#1	500
MCS-500μm-#2	MCS-#2	500
MCS-500μm-#3	MCS-#3	500
MCS-500μm-#4	MCS-#4	500
MCS-500μm-#5	MCS-#5	500

IV. POST-PROCESSING AND ANALYSIS OF RESULTS

A. Grid Convergence Study Analysis

i. Laín and Sommerfeld Minimum PSD Limit

To investigate grid convergence for all the particles within Laín and Sommerfeld's particle size distribution, a grid convergence study was conducted for the minimum and maximum particle sizes in the distribution. For the minimum particle size cases, pressure drops were found to converge for grid configurations MCS-#3 and MCS#4, showing under a 1% difference in the overall pressure drop when compared to MCS-#5. Similarly, volume fractions displayed under a 1% difference for MCS-#3 and MCS-#4. For particle velocities, the solutions showed difficulty in convergence, achieving approximately a 5% difference for MCS-#3 when compared with the finest grid configuration MCS-#5. Grid convergence solutions for pressure drop are shown in Figure 14, Figure 15, and Table 9.

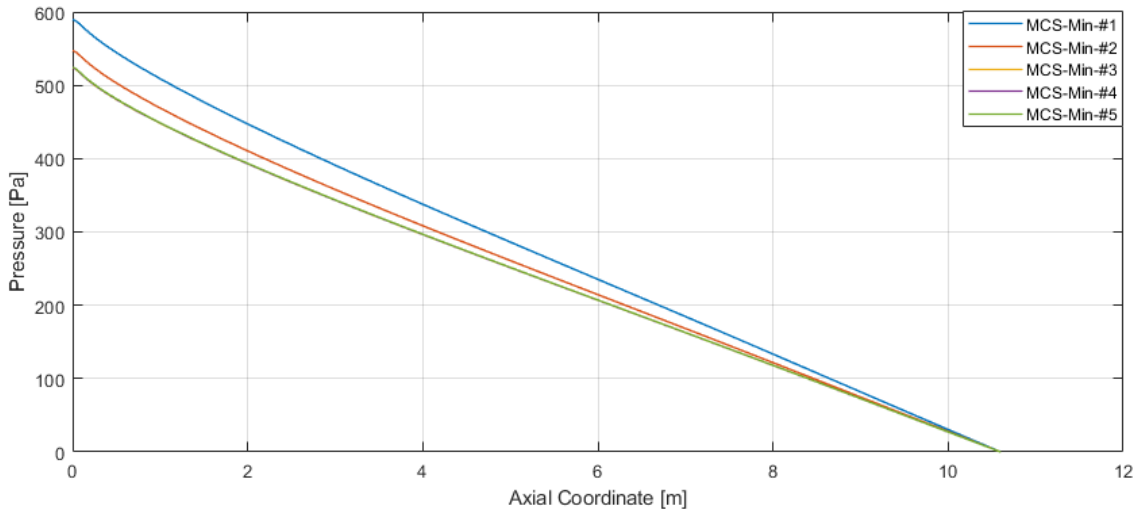

Figure 14: Pressure Drop Convergence for Minimum Particle Size

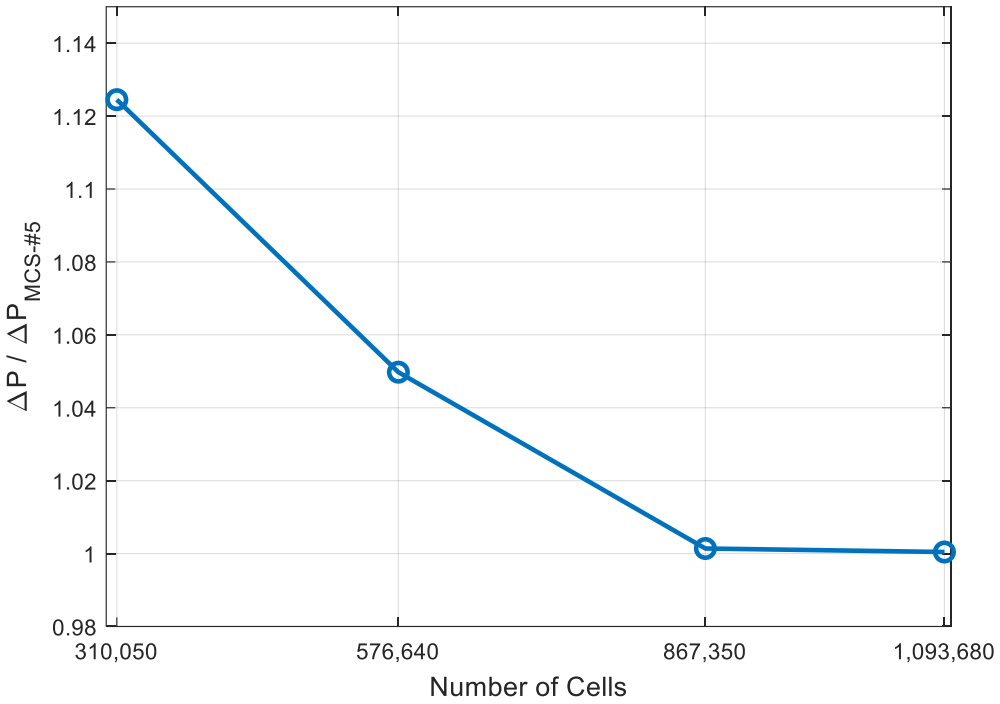

Figure 15: Pressure Convergence Analysis for Minimum Particle Range

Table 9: Pressure Drop Grid Difference for Minimum Particle Size Cases

Mesh Size	$\frac{\Delta P}{\Delta P_{MCS-\#5}}$
MCS-#1	1.12451
MCS-#2	1.04975
MCS-#3	1.00139
MCS-#4	1.00043

In Figure 14, pressure values obtained from the centerline of the geometry were plotted against the axial length of the pneumatic conveying pipe. Figure 15 and Table 9 depict the overall pressure drop difference between the grid sizes illustrated in Figure 14 against the finest grid size MCS-#5. For particle velocity profiles, convergence behavior was observed for the grid solutions shown in Figure 16-17 and Table 10:

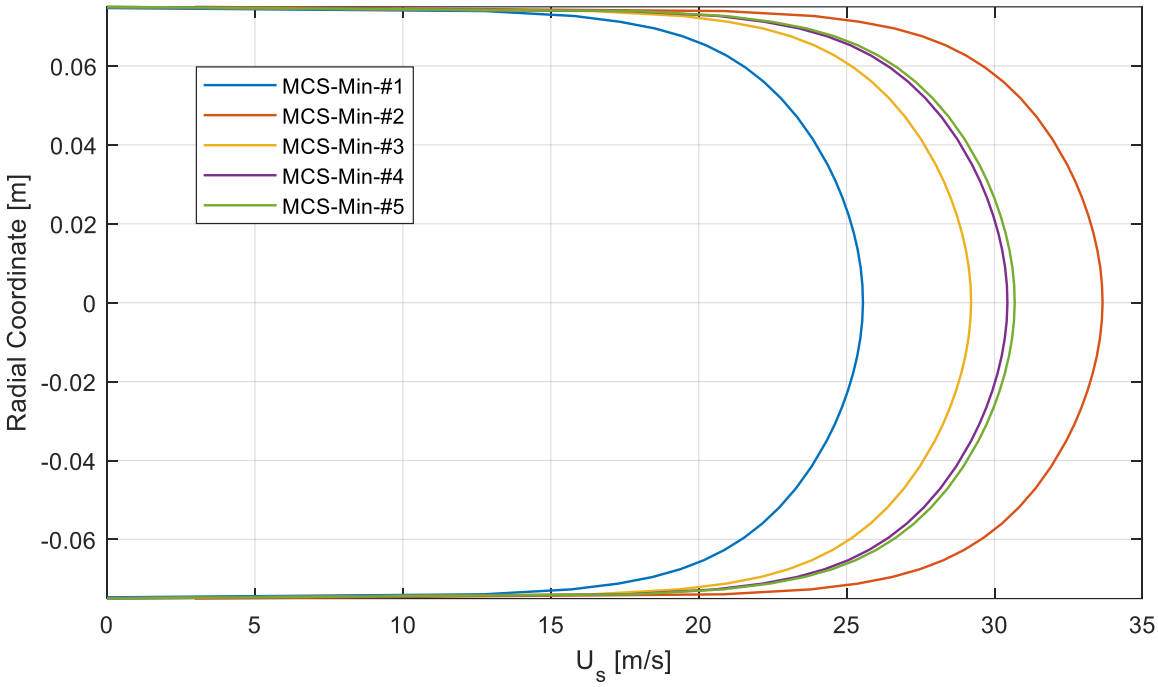

Figure 16: Velocity Grid Convergence for Minimum Particle Size

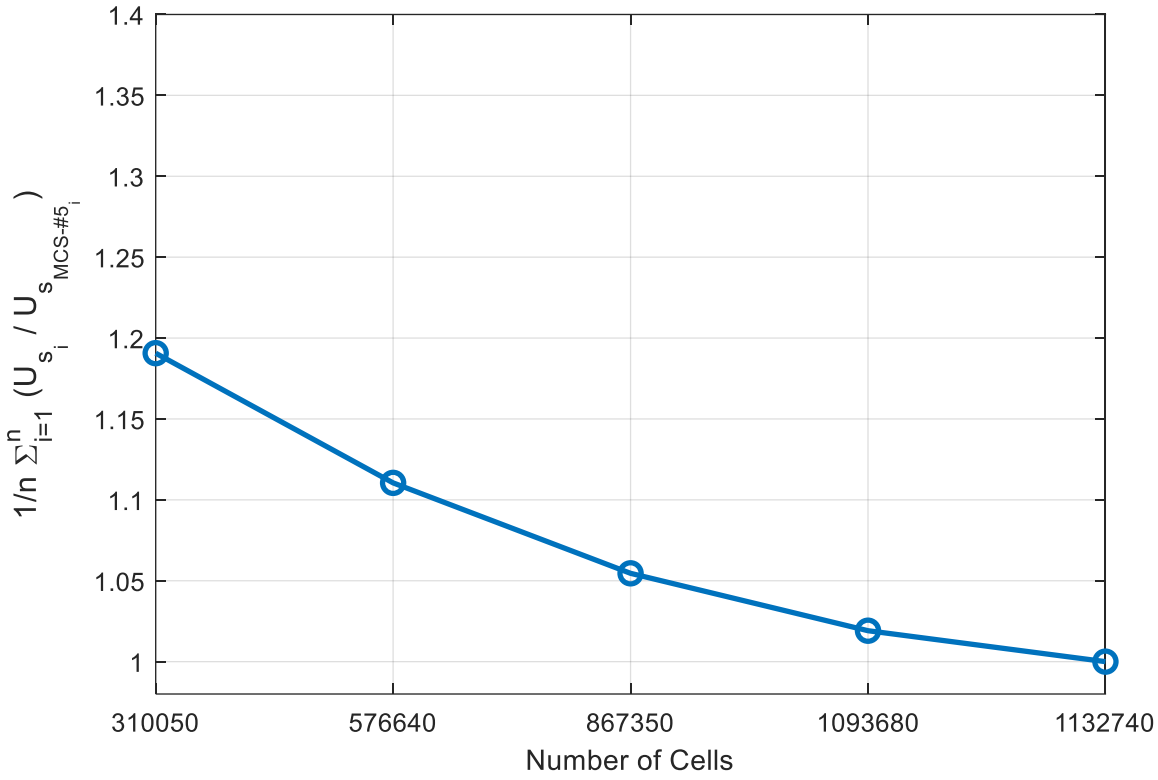

Figure 17: Velocity Convergence Analysis for Minimum Particle Range

Table 10: Particle Velocity Grid Difference for Minimum Particle Size Cases

Mesh Size	$\sqrt{\frac{1}{n}\sum_{i=1}^{n}\left(U_{s_i} - U_{s_{MCS-\#5_i}}\right)^2}$ (RMSD)	$\frac{1}{n}\sum_{i=1}^{n}\left\|\frac{U_{s_i}}{U_{s_{MCS-\#5_i}}}\right\|$
MCS-#1	5.2714	1.19065
MCS-#2	3.006	1.11049
MCS-#3	1.602	1.05459
MCS-#4	0.9771	1.01412

For particle velocities and volume fraction distributions, property data was extracted 8 m from the inlet. Figure 16 illustrates the particle velocity relative to the pipe's radial coordinate, while Table 10 and Figure 17 quantify the solution deviation from each mesh size case against the finest mesh. Volume fraction convergence solutions were extracted at the same 8 m location, shown in Figure 18-19 and Table 11:

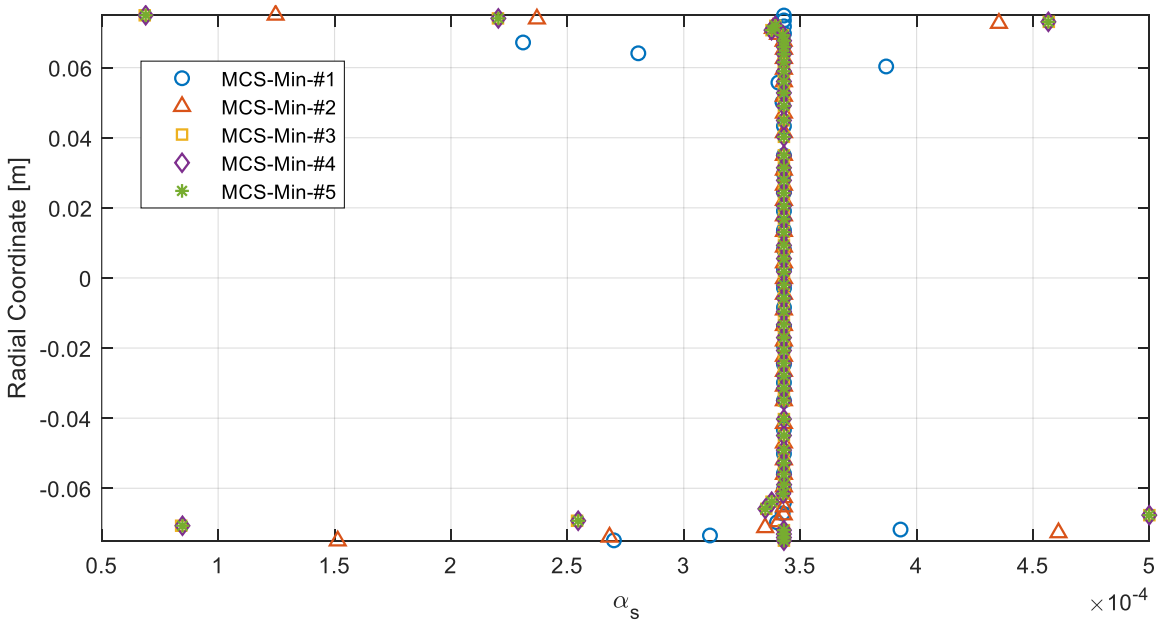

Figure 18: Volume Fraction Grid Convergence for Minimum Particle Size

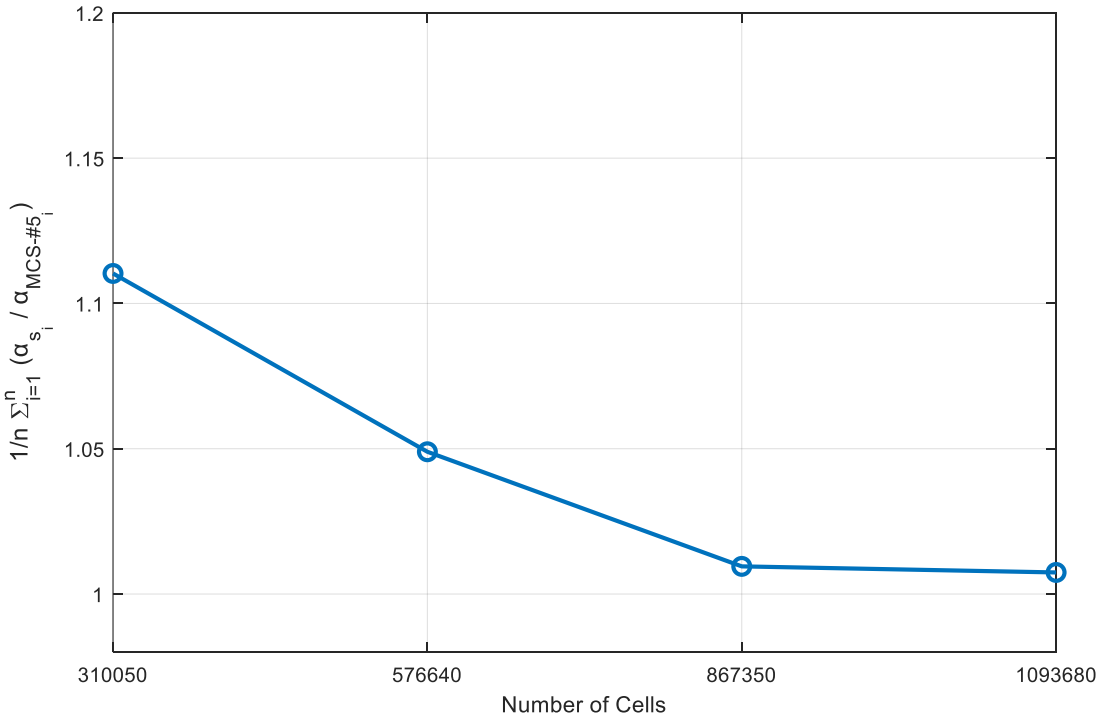

Figure 19: Volume Fraction Convergence Analysis for Minimum Particle Range

Table 11: Volume Fraction Grid Difference for Minimum Particle Size Cases

Mesh Size	$\sqrt{\frac{1}{n}\sum_{i=1}^{n}\left(\alpha_{s_i} - \alpha_{s_{MCS-\#5_i}}\right)^2}$ (RMSD)	$\frac{1}{n}\sum_{i=1}^{n}\left\|\frac{\alpha_{s_i}}{\alpha_{MCS-\#5_i}}\right\|$
MCS-#1	5.2378	1.11032
MCS-#2	3.3339	1.04896
MCS-#3	2.2183	1.00952
MCS-#4	0.9201	1.00743

. After evaluating pressure drop, particle velocities, and volume fractions using all grid configurations, it was found that MCS-#4 exhibited the closest agreement with MCS-#5, demonstrating deviations of approximately 1% for cases employing the minimum particle size range. Consequently, grid configuration MCS-#4 was selected as an ideal mesh for accurately describing all three flow parameters when employing the minimum particle sizes in the PSD.

ii. Laín and Sommerfeld Maximum PSD Limit

When examining grid convergence for the maximum particle size in the PSD, it was observed that pressure solution data converged showing errors of approximately 1% across all grid sizes tested, as depicted in Figure 20-21 and Table 12.

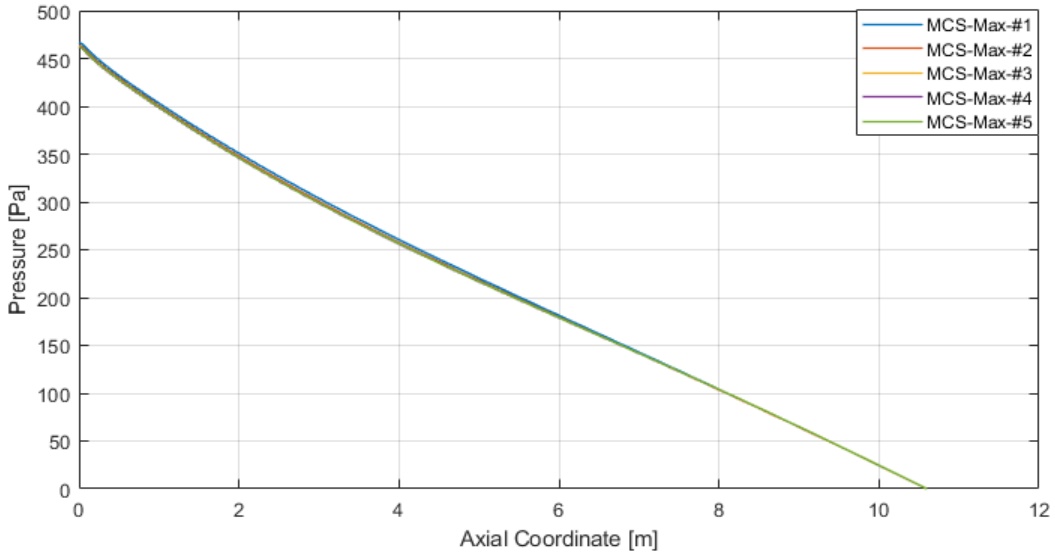

Figure 20: Pressure Drop Grid Convergence for Maximum Particle Size

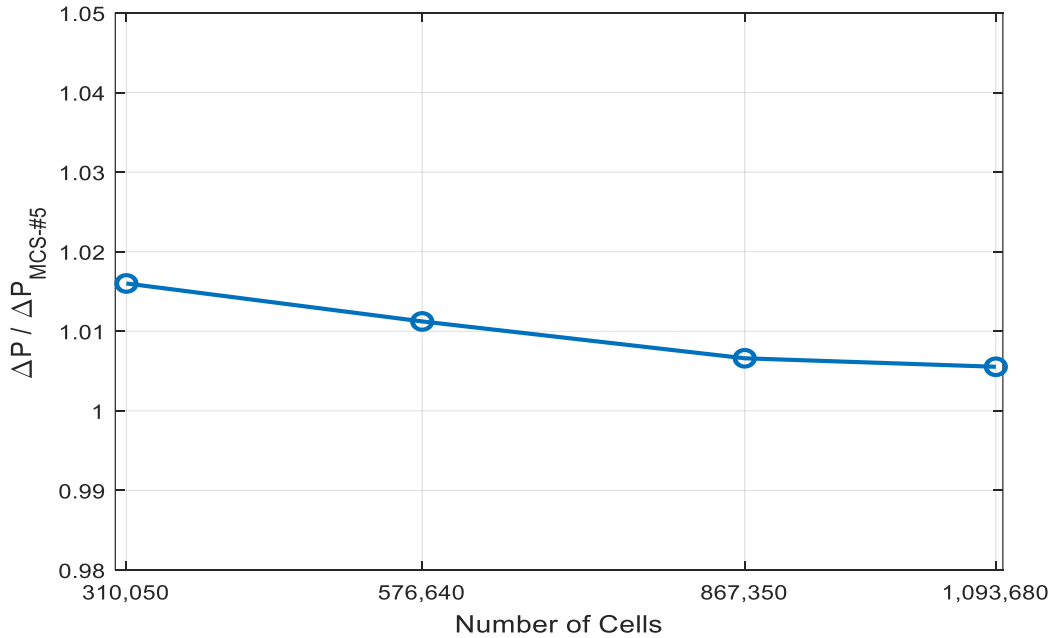

Figure 21: Pressure Convergence Analysis for Maximum Particle Range

Table 12: Pressure Drop Grid Difference for Maximum Particle Size Cases

Mesh Size	$\frac{\Delta P}{\Delta P_{MCS-\#5}}$
MCS-#1	1.01601
MCS-#2	1.01124
MCS-#3	1.00661
MCS-#4	1.00554

Pressure solutions gathered for all grid configurations gave rise to minimal deviations among each other. However, particle velocity and volume fraction solution data exhibited greater difficulty in reaching convergence, experiencing greater challenges compared to the minimum particle size cases. An average grid convergence agreement of about 2% could be achieved for particle velocity and volume fraction respectively, using grid configuration MCS-#4. Graphical and numerical depiction of these findings is shown below in Figure 22-23, Table 13 and Figure 24-25, Table 14 respectively.

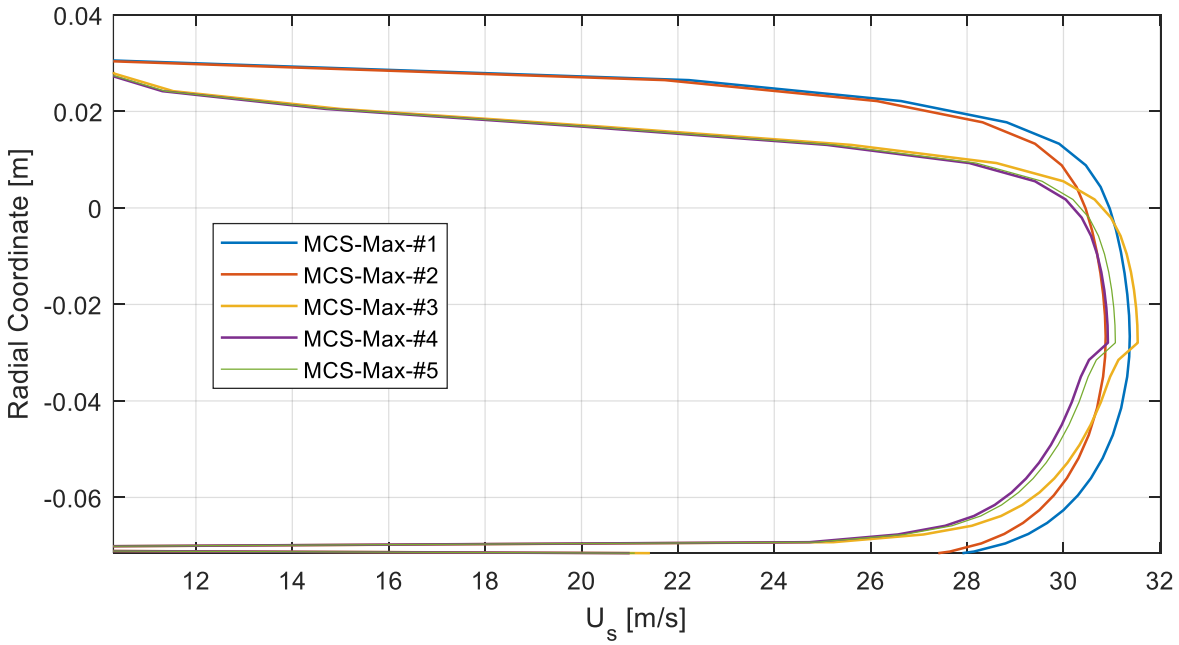

Figure 22: Velocity Grid Convergence for Maximum Particle Size

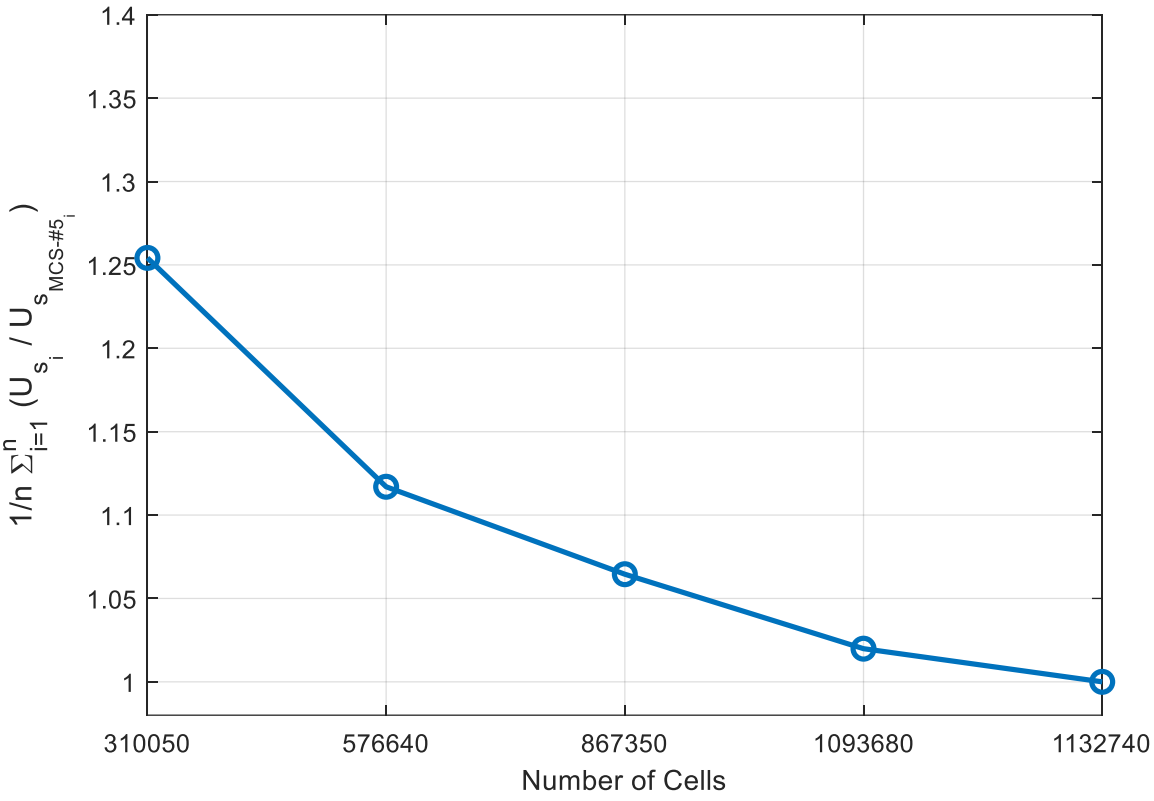

Figure 23: Velocity Convergence Analysis for Maximum Particle Range

Table 13: Particle Velocity Grid Difference for Maximum Particle Size Cases

Mesh Size	$\sqrt{\frac{1}{n}\sum_{i=1}^{n}\left(U_{s_i} - U_{s_{MCS-\#5_i}}\right)^2}$ (RMSD)	$\frac{1}{n}\sum_{i=1}^{n}\left\|\frac{U_{s_i}}{U_{s_{MCS-\#5_i}}}\right\|$
MCS-#1	7.3063	1.25421
MCS-#2	5.1355	1.11697
MCS-#3	4.6535	1.06453
MCS-#4	0.9125	1.01988

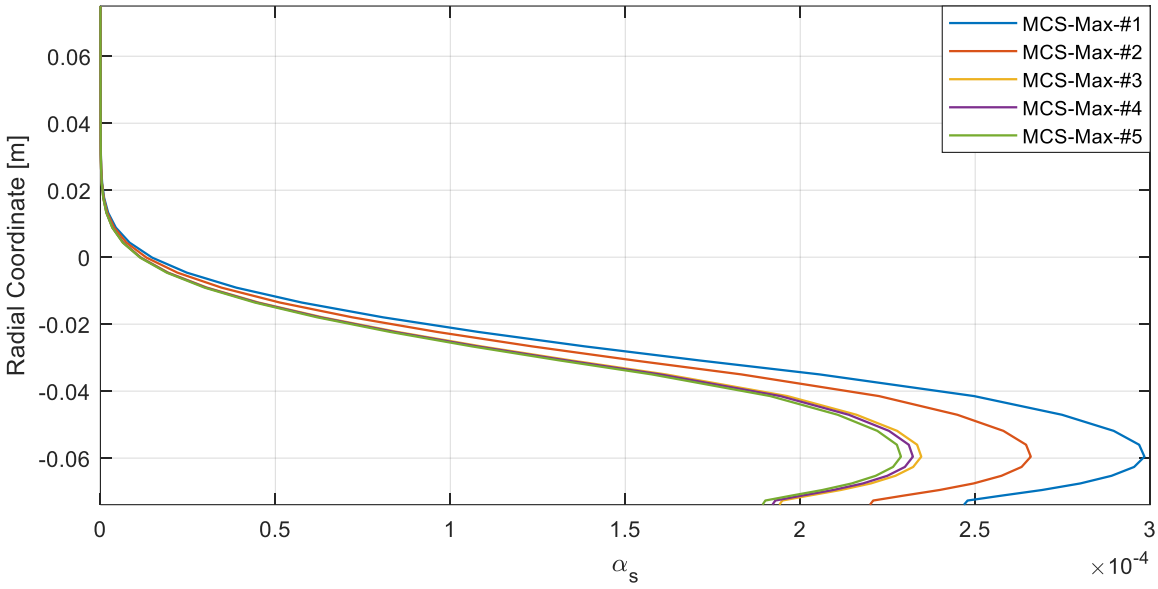

Figure 24: Volume Fraction Grid Convergence for Maximum Particle Size

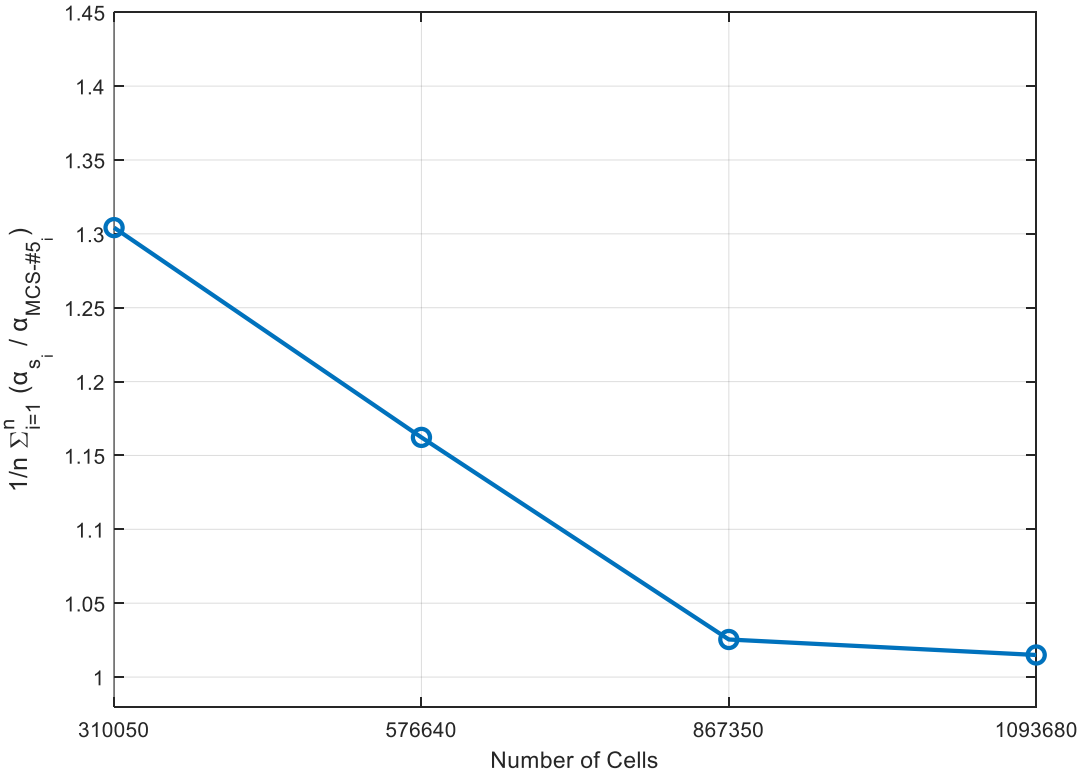

Figure 25: Volume Fraction Convergence Analysis for Maximum Particle Range

Table 14: Volume Fraction Grid Difference for Maximum Particle Size Cases

Mesh Size	$\sqrt{\frac{1}{n}\sum_{i=1}^{n}\left(\alpha_{s_i} - \alpha_{s_{MCS-\#5_i}}\right)^2}$ (RMSD)	$\frac{1}{n}\sum_{i=1}^{n}\left\|\frac{\alpha_{s_i}}{\alpha_{MCS-\#5_i}}\right\|$
MCS-#1	13.442	1.30421
MCS-#2	8.549	1.16222
MCS-#3	4.112	1.02543
MCS-#4	2.215	1.01495

Both grid convergence studies proved grid MCS-#4 as an optimal choice for accurately representing pressure drop, particle velocity, and volume fraction distributions across all minimum and maximum particle sizes within the PSD. Using this grid configuration, solution data could be gathered to validate the simulation using Laín and Sommerfeld's PSD and experimental results.

iii. PSD Study 500 µm Limit

Previous investigations into grid independence demonstrated that pressure drop solutions converged more effectively than volume fraction and particle velocity. Building upon these findings, a similar study was conducted to explore pressure solution grid convergence in a simulation featuring 500 µm diameter particles, encompassing the new maximum particle size established for the newly developed PSDs. This study enabled the generation of additional PSDs to assess how different characterizations of the distribution influenced pressure drop solutions.

In this grid convergence study, MCS-#2 and MCS-#3 configurations showed differences below 5% in the overall pressure drop within the pneumatic system, respectively. Grid configuration MCS-#4 exhibited an even smaller difference under 1%, justifying the selection of the fourth grid configuration to represent both Laín and Sommerfeld's PSD and the newly developed PSDs introduced in this study. Pressure convergence data for 500µm case study is shown in Figure 26-27 and Table 15.

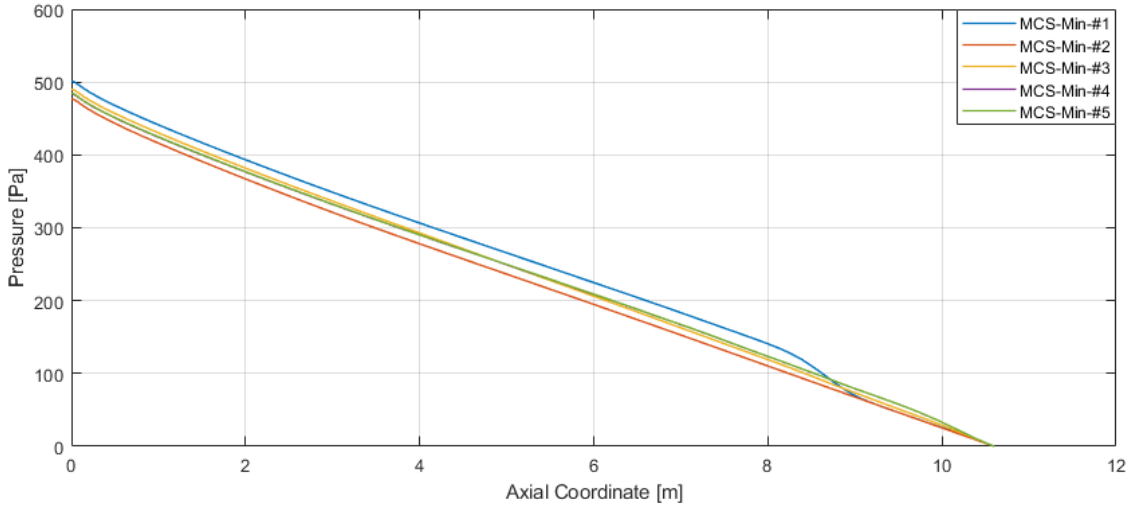

Figure 26: Pressure Drop Grid Convergence for 500µm Particle Size

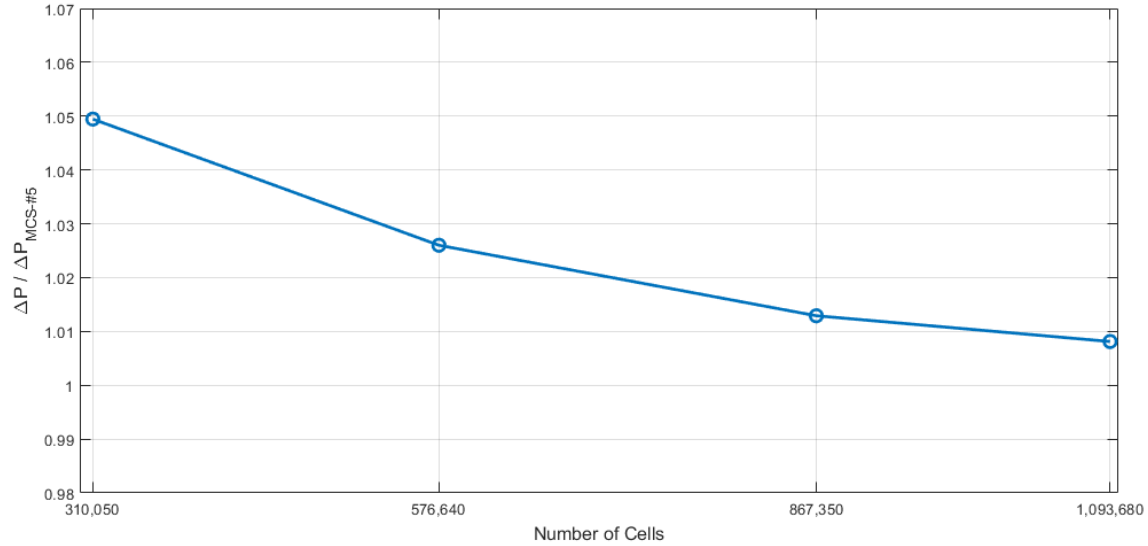

Figure 27: Pressure Convergence Analysis for 500µm Particle Size Range

Table 15: Pressure Drop Grid Difference for 500μm Particle Size Cases

Mesh Size	$\frac{\Delta P}{\Delta P_{MCS-\#5}}$
MCS-#1	1.04945
MCS-#2	1.02601
MCS-#3	1.01291
MCS-#4	1.00812

B. Laín and Sommerfeld Model Validation and Bin analysis.

i. Proposed Eulerian-Eulerian Model Validation

When comparing the overall pressure drop between Laín and Sommerfeld experimental data and the simulation results, reasonable agreement was observed between the two datasets, as depicted in Figure 28 and Table 16.

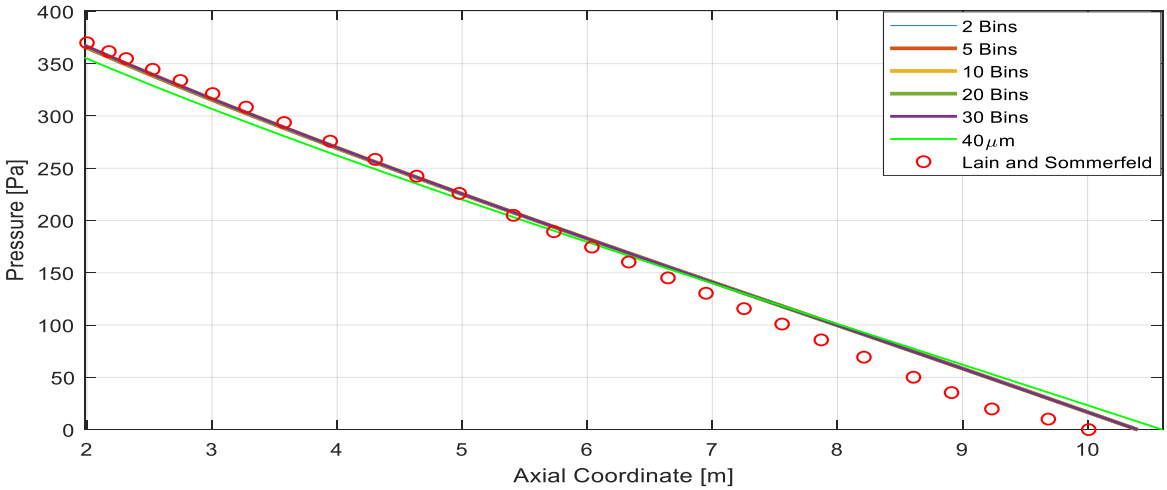

Figure 28: Pressure Drop for Polydisperse and Monodisperse Cases

Table 16: Pressure Model Validation for Monodisperse and 30-Bin Cases

Case	$\frac{\Delta P - \Delta P_{Lain}}{\Delta P_{Lain}} * 100\ (\%)$
$40\mu m$	4.054
30-Bin	0.9189

The first 40 µm monodisperse case representing the mean diameter obtained from Laín's PSD displayed pressure drop variations under 5%. For the polydisperse 30-bin case, this pressure drop difference was reduced to under 1%. Through these findings, the 30-bin polydisperse case proved to give rise to higher accurate pressure drop predictions than the monodisperse mean diameter case. However, the pressure drop prediction revealed a difference of only about 3% between the monodisperse and polydisperse cases. This finding further emphasized the practicality of representing the polydisperse mixture as monodisperse when predicting pressure drop profiles in pneumatic conveying systems operating with a similar PSD range, particularly when such a deviation is deemed acceptable.

The characterization of larger particle sizes in Laín and Sommerfeld's PSD via bins led to a notable surge in pressure drop within the system compared to the 40 µm case. This increase could be attributed to the increase in frictional resistances created by the interaction of larger particle's surface areas with the pipe walls and the gaseous phase. This effect could not be described adequately in the 40 µm monodisperse case, given its constraint of describing all particles as the same size.

Apart from pressure drop predictions, the viability of the proposed model for predicting particle velocities and volume fraction distributions was tested. For this

section, particle velocities and volume fractions were normalized using the same normalization parameters given in Laín and Sommerfeld's and Huber and Sommerfeld's pneumatic conveying studies [6-7]. The particle velocity (U_s) was normalized by the average velocity at the inlet ($U_{av} = 27\frac{m}{s}$) and the volume fractions were used to find and normalize the particle mass flux (f_p). The radial coordinates were also normalized using the pipe radius ($R = 75mm$). These normalization techniques allowed for the creation of normalized particle velocity and particle mass flux profiles that could be compared with the experimental data provided. Graphical comparisons between experimental and simulated results for both flow parameters are shown in Figure 29-30:

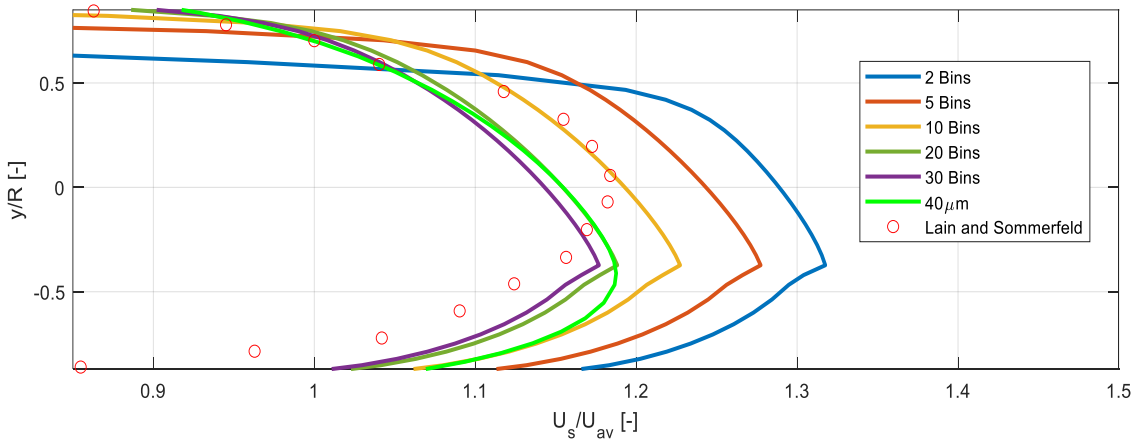

Figure 29: Particle Velocity Profiles for Polydisperse and Monodisperse Cases

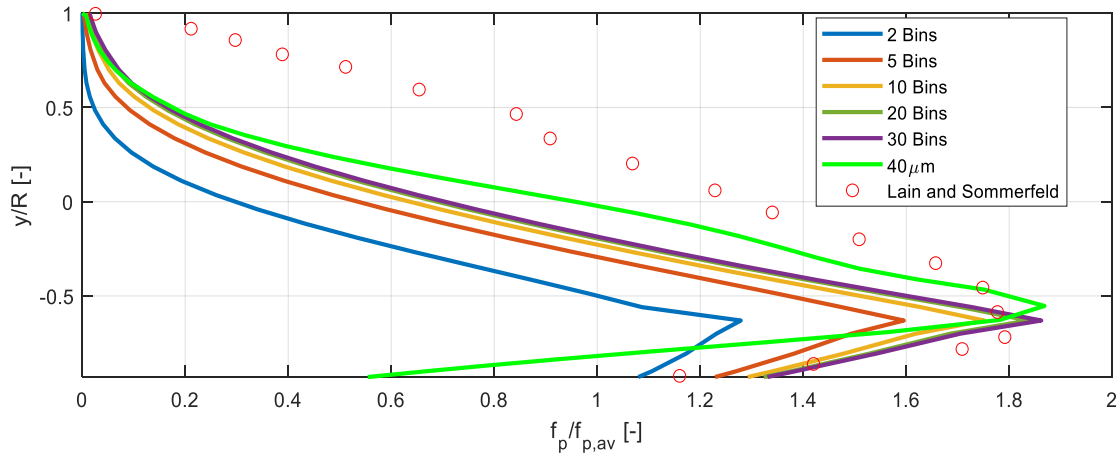

Figure 30: Particle Mass Flux Profiles for Polydisperse and Monodisperse Cases

The sharp discontinuity in Figure 30 was attributed to the representation of the sharp interface between the solid and fluid phases [35]. Discontinuities in mass fluxes arose from inaccuracies in the volume fraction fields near this interface, where sharp transitions occurred between regions dominated by solid particles and those dominated by the fluid phase. To account for each bin, multiple continuous secondary phases were also created in the simulation, which introduced further complexity in the interface region between adjacent phases, impacting the sharp transitions between them. This was particularly relevant in the studied dilute flow regime, where rapid changes in phase properties occurred over small spatial distances.

Furthermore, the representation of particle sizes through bins had a significant impact on the velocity and mass flux profiles, as shown in Figures 29-30. When increasing the number of bins used in the polydisperse simulation, it was found that the particle velocities decreased while the particle mass flux profiles increased. The phenomenon observed, where an increase in mass flux profiles coincided with a decrease in particle velocities in polydisperse simulations with an increased number of bins, may initially seem paradoxical. However, this behavior could be attributed to the finer bin resolution enabling a more accurate representation of particle sizes within the system. As the number of bins was increased, a broader range of particle sizes, including larger particles with lower velocities, were accounted for in the simulation. Similarly, individual particle velocities may decrease, but the overall mass flux could have increased due to the inclusion of larger particles contributing to a greater mass concentration within the lower regions of the pipe.

From these analyses, the modeled normalized particle velocity solutions exhibited a deviation of 4.1% for the monodisperse case and 3.8% for the 30-bin polydisperse case when compared to experimental results. However, the normalized mass fluxes for both cases showed higher averaged deviations, reaching up to 40.1% for the monodisperse case and 37.4% for the 30-bin polydisperse case. These findings indicated that, while the Eulerian-Eulerian model was able to accurately quantify pressure drop within the system, it had limitations in predicting particle velocities and mass fluxes. However, the predicted particle velocities and volume fraction profiles remained similar in nature to those obtained experimentally, demonstrating the potential of the model to provide insights into the behavior of these properties. Error analysis for particle velocity and volume fraction for the monodisperse and 30-bin polydisperse case compared to Laín and Sommerfeld's experimental data is provided in Table 17 and Table 18 respectively.

Table 17: Velocity Model Validation for Monodisperse and 30-Bin Cases

Case	$\frac{1}{n}\sum_{i=1}^{n}\frac{\left\lvert\frac{U_{s_i}}{U_{av_i}}-\frac{U_{s_{Lain_i}}}{U_{av_{Lain_i}}}\right\rvert}{\frac{U_{s_{Lain_i}}}{U_{av_{Lain_i}}}} * 100\ (\%)$
$40\mu m$	4.127
30-Bin	3.809

Table 18: Mass Flux Model Validation for Monodisperse and 30-Bin Cases

Case	$\frac{1}{n}\sum_{i=1}^{n}\frac{\left\lvert\frac{f_{p_i}}{f_{p,av_i}}-\frac{f_{p_{Lain_i}}}{f_{p,av_{Lain_i}}}\right\rvert}{\frac{f_{p_{Lain_i}}}{f_{p,av_{Lain_i}}}} * 100\ (\%)$
$40\mu m$	40.0796
30-Bin	37.388

Apart from validating the model's capabilities for predicting the mentioned flow parameters, a bin convergence study was conducted for the polydisperse cases. When prescribing bins to the polydisperse mixture, it was found that particle velocity and volume fraction solutions were more sensitive to the number of bins selected than pressure drop. Between the 20-bin and 30-bin cases, only a 0.9% difference was observed in pressure drop solutions. Particle velocity and mass flux solutions reached bin convergence after more bins were used, showing average deviations of 3.3% and 4.1% respectively compared to the 30-bin case when using 20 bins. Based on these findings, it was determined that the optimal number of bins required to accurately represent Laín and Sommerfeld's PSD fell within the range of 20 to 30-bins. Within this range, velocity and mass flux solution deviations were predicted to reduce to under 5%, a level of accuracy that may be acceptable depending on the design constraints of the pneumatic conveying system under study. The bin convergence findings for pressure, particle velocity and mass flux solutions are shown in greater detail in Table 19:

Table 19: Bin Convergence Study Using Laín's PSD

Case	$\frac{\Delta P-\Delta P_{Bin30}}{\Delta P_{Bin30}} * 100\ (\%)$	$\frac{1}{n}\sum_{i=1}^{n}\frac{\left\lvert\frac{U_{s_i}}{U_{av_i}}-\frac{U_{s_{Bin30_i}}}{U_{av_{Bin30_i}}}\right\rvert}{\frac{U_{s_{Bin30_i}}}{U_{av_{Bin30_i}}}} * 100\ (\%)$	$\frac{1}{n}\sum_{i=1}^{n}\frac{\left\lvert\frac{f_{p_i}}{f_{p,av_i}}-\frac{f_{p_{Bin30_i}}}{f_{p,av_{Bin30_i}}}\right\rvert}{\frac{f_{p_{Bin30_i}}}{f_{p,av_{Bin30_i}}}} * 100\ (\%)$
2-Bins	5.365	31.335	45.634
5-Bins	3.648	14.334	16.733
10-Bins	1.193	5.957	6.334
20-Bins	0.873	3.273	4.135

The sensitivity observed in the prescription of additional bins for particle velocity and mass flux parameters, not discernible in pressure solutions, can be attributed to the influence of particles on the examined flow. For this scenario involving particle sizes ranging approximately from 1 μm to 100 μm operating within a dilute flow regime, the contribution of particles to the overall pressure drop in the system becomes nearly negligible. This is because the particulate phase exerts only a minimal influence on the gaseous phase under these conditions, due to the minimal concentrations and surface areas of the particles interacting with the gaseous phase.

While the solid phase has a slight influence on the fluid carrier phase, the gaseous phase predominantly dictates the dynamics of the particulate phase under these conditions. Following Stokes number principles, larger particles tend to track the fluid carrier less closely and exhibit more independent trajectories, whereas smaller particles readily disperse and mix with the gaseous phase. The Stokes number plays a significant role in flow characterization, as it considers both fluid and particle properties, with particle diameter being a critical factor to consider. As larger particle sizes are represented by more bins, the Stokes number would increase, resulting in a larger difference in the particle's flow behavior.

Given that particle flow behavior is highly influenced by particle size, accurately characterizing particle sizes within the studied PSD is crucial for capturing the significant influence of the gaseous phase on the particulate phase, as well as the particulate phase's resistance to it. This reasoning explains the phenomena of why more bins were required to accurately portray particle velocity and mass flux solutions, reflected in Table 19.

ii. Mean Diameter PSD Characterization Study

After comparing the 40 µm monodisperse case with experimental data, a new set of monodisperse cases using mean diameter expressions to represent the polydisperse nature of the mixture were conducted. The arithmetic mean, surface area mean, volume mean, Sauter mean and De Brouckere mean diameters for Laín and Sommerfeld's PSD were calculated and used to set the particle sizes in the simulations. Laín and Sommerfeld's calculated mean diameters are shown below in Table 20:

Table 20: Mean Diameters for Laín and Sommerfeld PSD

Mean Diameter	Value [µm]
Arithmetic Mean (d_{10})	40.0000
Surface Area Mean (d_{20})	43.1341
Volume Mean (d_{30})	45.7067
Sauter Mean (d_{32})	51.2808
De Brouckere (d_{43})	56.2823

The arithmetic mean provided a measurement of the average size of particles in the distribution, giving equal weight to each particle [36]. The surface area mean emphasized on describing surface effects like friction due to the interaction of particle's surface areas. The volume mean assisted in representing the volume occupied by the

particles, providing insights into the overall size of the particles and the space they occupied within the system. In addition, the Sauter mean diameter was able to provide a better volume to surface ratio estimation than the volume mean expression to represent an average diameter size from the PSD. Lastly, De Brouckere mean diameter definition was used to account for the skewness of the PSD [33]. Formulaic expressions for each mean diameter definitions are provided in Table 21:

Table 21: Mean Diameter Expressions

Mean Diameter	Formula
Arithmetic Mean (d_{10})	$d_{10} = \frac{1}{N}\sum_{i=1}^{N} d_i$
Surface Area Mean (d_{20})	$d_{20} = \left(\frac{\sum_{i=1}^{N} d_i^2}{N}\right)^{\frac{1}{2}}$
Volume Mean (d_{30})	$d_{30} = \left(\frac{\sum_{i=1}^{N} d_i^3}{N}\right)^{\frac{1}{3}}$
Sauter Mean (d_{32})	$d_{32} = \left(\frac{\sum_{i=1}^{N} d_i^3}{\sum_{i=1}^{N} d_i^2}\right)$
De Brouckere (d_{43})	$d_{43} = \left(\frac{\sum_{i=1}^{N} d_i^4}{\sum_{i=1}^{N} d_i^3}\right)$

Using the mean diameter expressions shown in Table 21, pressure drop, particle velocity and mass flux solution accuracies were investigated and compared to the 30-bin case. Among the mean diameters, the Sauter mean diameter displayed the most

agreement in pressure drop solutions with the 30-bin case, with De Brouckere, volume mean, surface area mean and arithmetic mean following respectively. The higher pressure drop observed in the Sauter and De Brouckere mean diameter cases were attributed to their accurate characterization of the effects of larger particles on pressure variations, consistent with the results obtained in the 30-bin case. While the De Brouckere mean diameter reflected larger particle sizes, the Sauter mean diameter was able to effectively capture the interplay between particle sizes and particle concentrations in the PSD, and their effects on pressure changes in the system. Pressure drop results showed variances ranging from 0.86% to 1.6% compared to the 30-bin case. Pressure drop solution for the 30-bin case compared to the mean diameter cases is shown in Figure 31:

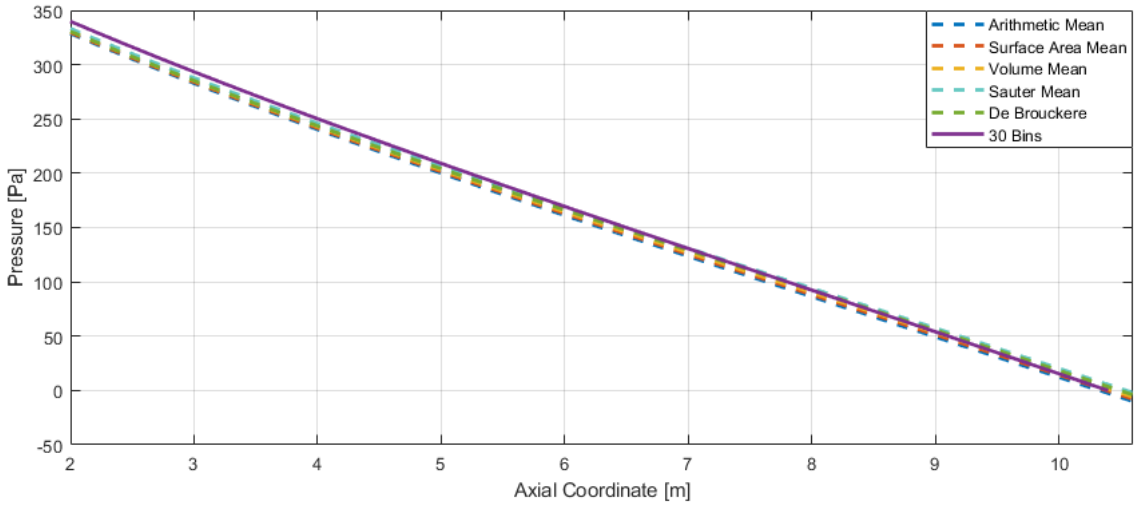

Figure 31: Mean Diameter Pressure Drop Solution Using Laín's PSD

Mean diameter particle velocities exhibited low solution sensitivity as well, ranging from 1.8% to 2.6% when compared to the 30-bin case. Similar to pressure drop solutions, the Sauter mean diameter displayed the most agreement in particle velocity solutions with the 30-bin case, with De Brouckere, volume mean, surface area mean, and arithmetic mean following respectively. The Sauter mean and De Brouckere mean diameters yielded slower velocity profiles compared to other mean diameters due to their larger average particle sizes, resulting in greater mass and increased resistance to acceleration within the conveying system. The arithmetic mean diameter resulted in the highest peak velocities due to its smaller mean particle size, making it more responsive to changes in flow velocity within the pneumatic conveying system. Particle velocity solutions for all mean diameter cases are shown in Figure 32(a) and Figure 32(b).

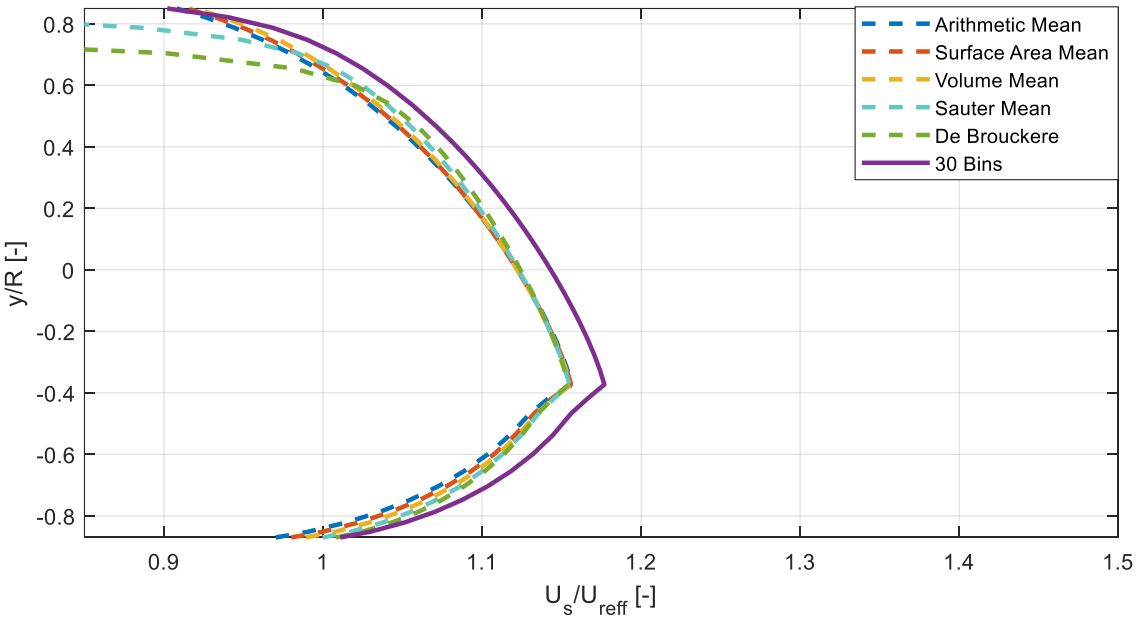

Figure 32(a): Mean Diameter Particle Velocity Solution Using Laín's PSD

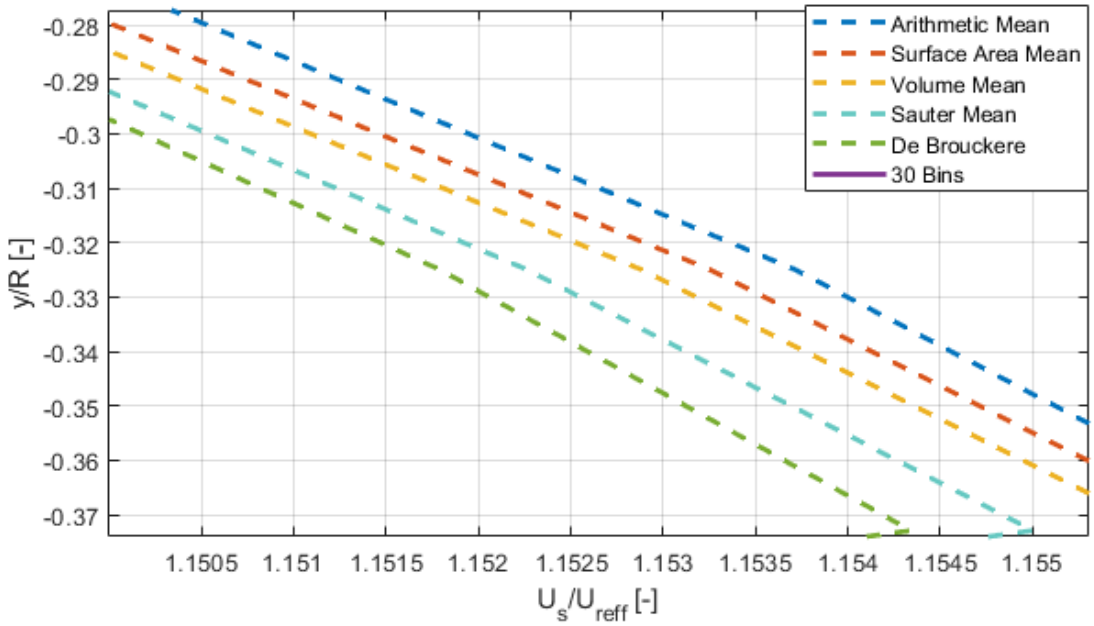

Figure 32(b): Magnified Mean Diameter Particle Velocity Solution

Even though there were minimal solution variations for pressure drop and particle velocities, mass flux solutions exhibited higher disparities, ranging from 4.4% to 15.4% difference. The Sauter mean mass flux solution showcased the highest agreement with the 30-bin case, with the following mean diameters solutions behaving in the same manner as in pressure drop and particle velocity solutions.

The arithmetic mean diameter yielded the highest mass flux values, contrasting with the De Brouckere mean diameter, which resulted in the lowest. This distinction stemmed from the respective mean particle sizes in each case. Although the De Brouckere particle size of 56 µm exceeded the arithmetic mean particle size of 40 µm, the disparity was not significant enough to substantially alter the mass fluxes in the system due to additional mass contributions by the larger particles. In this scenario, the mass fluxes were primarily influenced by the velocity experienced by each particle. Therefore, despite its smaller particle size, the arithmetic mean diameter exhibited higher mass

fluxes due to the larger flow rate of particles in the system. This trend can be observed for mass flux solutions in Figure 33:

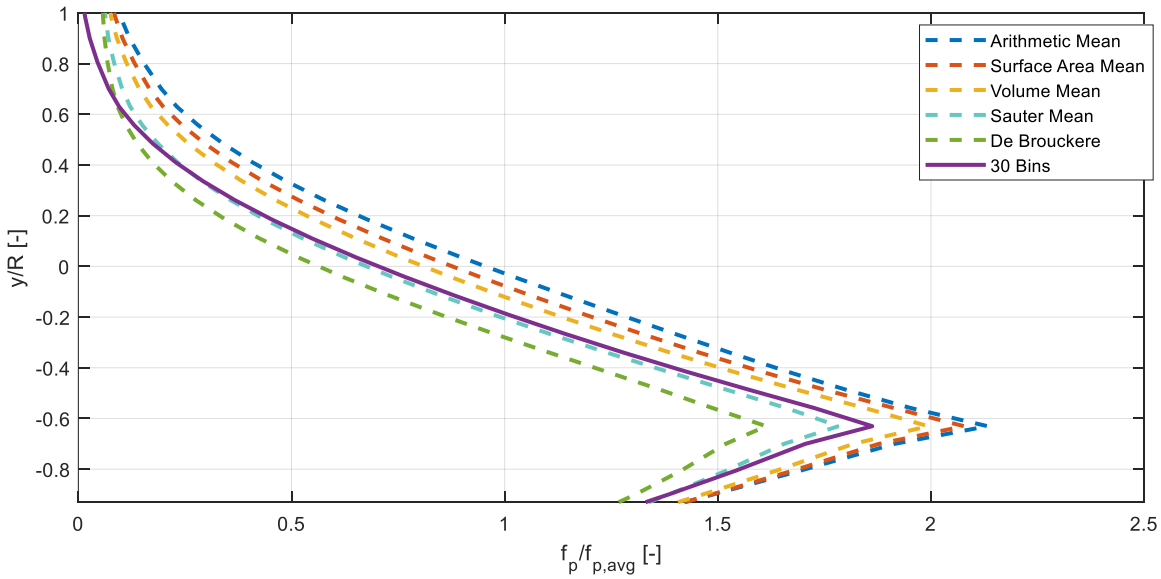

Figure 33: Mean Diameter Mass Flux Solution Using Laín's PSD

Based on this study, it was revealed that certain mean diameter expressions could lead to deviations in particle velocity and mass flux solutions of less than 5% for the particle size distribution studied. Utilizing these expressions primarily for pressure drop predictions would be more advantageous, as they consistently yielded predictions with differences of under 1%. A quantifiable representation of the deviation between these solutions is shown in Table 22.

Table 22: Mean Diameter Analysis compared to 30-Bin Case

Case	$\frac{\Delta P - \Delta P_{Bin30}}{\Delta P_{Bin30}} * 100$ (%)	$\frac{1}{n}\sum_{i=1}^{n}\frac{\left\lvert\frac{U_{S_i}}{U_{av_i}} - \frac{U_{S_{Bin30_i}}}{U_{av_{Bin30_i}}}\right\rvert}{\frac{U_{S_{Bin30_i}}}{U_{av_{Bin30_i}}}} * 100$ (%)	$\frac{1}{n}\sum_{i=1}^{n}\frac{\left\lvert\frac{f_{p_i}}{f_{p,av_i}} - \frac{f_{p_{Bin30_i}}}{f_{p,av_{Bin30_i}}}\right\rvert}{\frac{f_{p_{Bin30_i}}}{f_{p,av_{Bin30_i}}}} * 100$ (%)
Arithmetic Mean	1.648	2.609	15.437
Surface Area Mean	1.445	2.165	12.677
Volume Mean	1.392	1.834	10.354
Sauter Mean	0.855	1.773	4.446
De Brouckere	1.173	1.804	6.595

The consistency of this modeling approach for predicting pressure within a system could be further tested by applying it to a wider range of particle size distributions. This expanded testing would validate the applicability and robustness of the modeling technique for predicting pressure across varying particle size distributions within the studied pneumatic conveying simulation.

C. Particle Size Distribution Bin Variance Analysis

In this study, analyses were conducted for four particle size distributions to investigate bin convergence and to validate the usage of mean diameter expressions for representing the polydisperse mixture. Previously in this investigation, Table 5 highlighted the standard deviations and mean values attributed to each PSD established.

In the bin convergence studies, it was observed that simulations with smaller particle mean diameters tended to converge with fewer bins. For instance, PSD #3 reached bin convergence with fewer bins compared to PSD #1, and PSD #1 solutions converged with fewer bins than PSD #2. This trend was also reflected in the accuracy of mean diameter expressions for predicting pressure drop compared to the 30-bin case for each PSD. This behavior is shown in Figure 34.

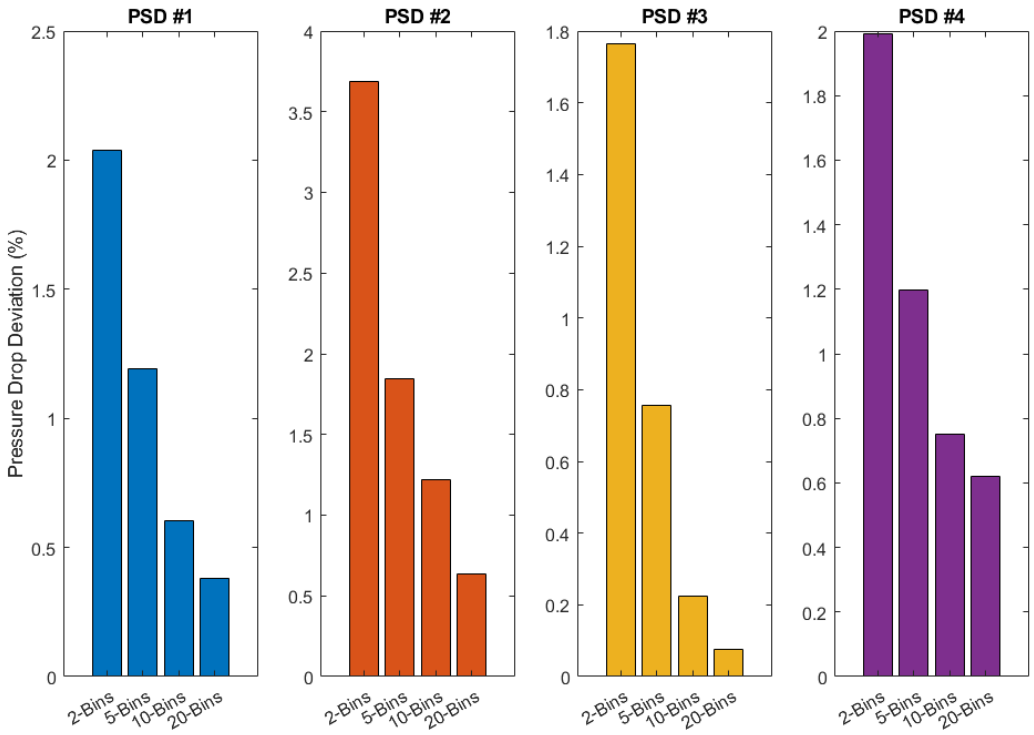

Figure 34: Bin Convergence Comparison for PSDs

Across all mean diameter expressions studied for each PSDs, the Sauter Mean diameter was found to be the most accurate mean diameter expression for predicting pressure solutions, followed by the De Brouckere, volume mean, surface area mean, and arithmetic mean respectively. PSD #3, which had the smallest particle size mean, exhibited less deviation in mean diameter solutions for all expressions. Similarly, PSD #1 demonstrated a smaller deviation in mean diameter solutions compared to its 30-bin case than PSD #2.

One plausible explanation for the enhanced accuracy in predicting pressure solutions when dealing with smaller particles in the PSD could be attributed to the simplicity of capturing all the pressure drop effects within that distribution. For particle size distributions where all particles within the distribution are relatively small, these particles would exert less influence on pressure drop results. Within these distributions comprised of smaller particles, capturing the dominant particle size which would exhibit significant pressure effects becomes more manageable with fewer bins and with a single mean diameter size. This is because only a minimal concentrated fraction of the mixture, comprising larger particles, significantly contributes to the pressure-varying effects on the system, while the smaller particle's contribution becomes nearly inconsequential. In contrast, with PSDs containing larger particle sizes, it becomes more challenging to accurately capture the pressure effects caused by all particles. In such cases, not only does one small concentration of particle sizes dominate the pressure drop effects, but all particle sizes contribute to determining the overall impact.

Apart from investigating solution variance when using multiple particle sizes for PSDs, the study explored the effectiveness of the modeling technique in capturing

simulation solutions for two distribution patterns. When comparing single-peak PSD #1 and three-peak PSD #4, it became apparent that the choice of mean diameter expression was influenced by the way particle sizes were distributed. Despite PSD #4 sharing the same mean distribution as PSD #1, it exhibited higher deviations in mean diameter simulations compared to its 30-bin case. This disparity was attributed to the complex distribution of PSD #4, which divided particle sizes into three distinct regions rather than in a single peak. Additionally, PSD #4 showed larger errors in certain mean diameter expressions, particularly when using the arithmetic mean diameter. Recall that the arithmetic mean diameter is intended to capture the average size of particles within the simulation space, regardless of their distribution. However, because PSD #4 exhibited a more complex distribution consisting of both larger and smaller particles, the arithmetic mean diameter failed to accurately represent the variations in particle sizes observed in the simulation.

Overall, the mean diameter expressions tested for all PSDs showed minimal deviation differences compared to each 30-bin case, with a maximum error of 1.6% observed for the arithmetic mean expression in PSD #4. Considering that the simulated particle sizes remained within the micron range and adhered to the prescribed dilute flow regime, their impact on pressure drop was relatively small. However, this study showcased the potential of using the Sauter Mean diameter to predict pressure drop for polydisperse mixtures encompassing particle sizes within the investigated ranges, as illustrated in Figure 35:

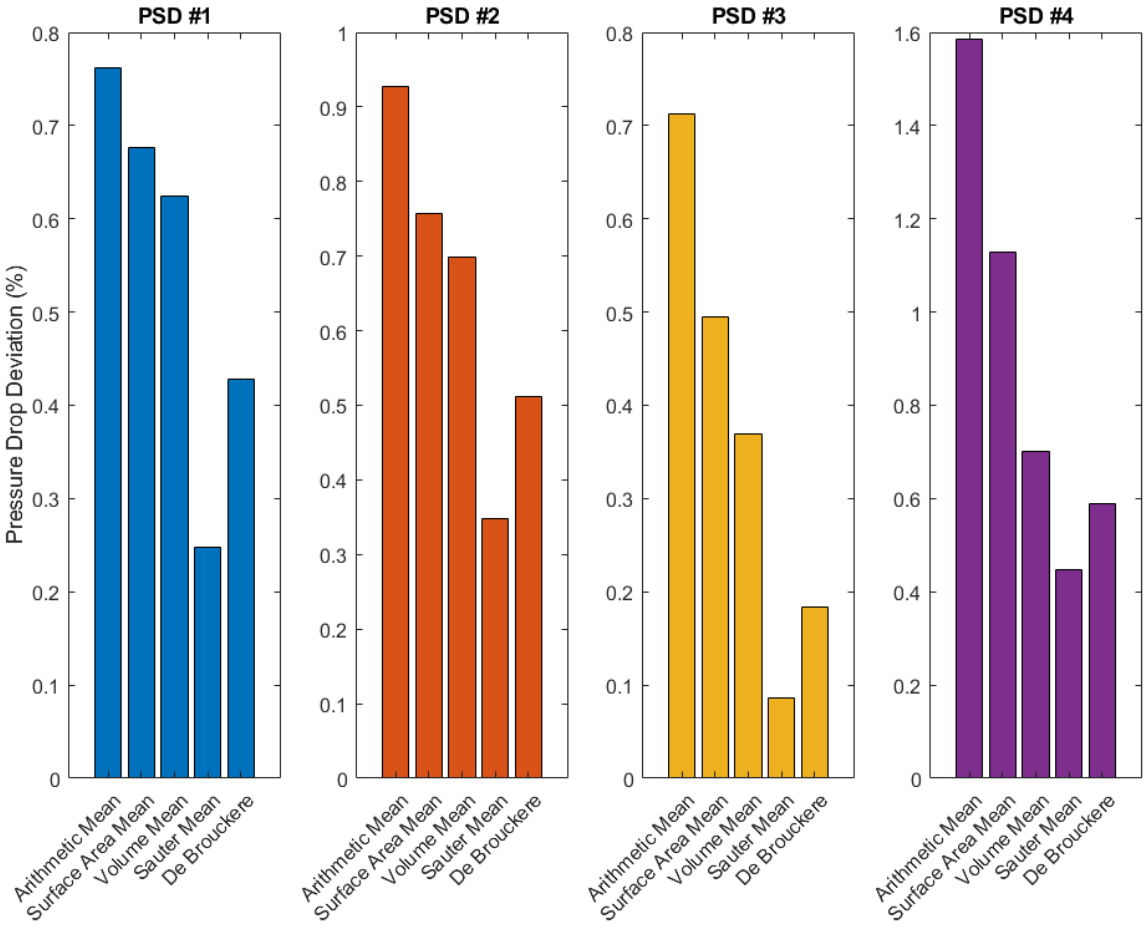

Figure 35: Mean Diameter Comparison for PSDs

i. Particle Size Distribution Analysis #1

For the first PSD studied, the optimal bin number for accurately predicting pressure drop fell within the range of 10 to 20 bins. Solutions obtained within this range were expected to show less than a 1% difference, with an acceptable RMSD value below 1 for the collected data. Table 23 illustrates the bin convergence results for the first PSD. Figure 36 displays the pressure drop solutions obtained for each bin.

Table 23: Bin Convergence Study for PSD #1

Case	$\sqrt{\frac{1}{n}\sum_{i=1}^{n}(P_i - P_{Bin30})^2}$ (RMSD)	$\frac{\Delta P - \Delta P_{Bin30}}{\Delta P_{Bin30}} * 100$ (%)
2-Bins	4.4212	2.0363
5-Bins	2.0938	1.1933
10-Bins	0.9179	0.6026
20-Bins	0.3646	0.3814

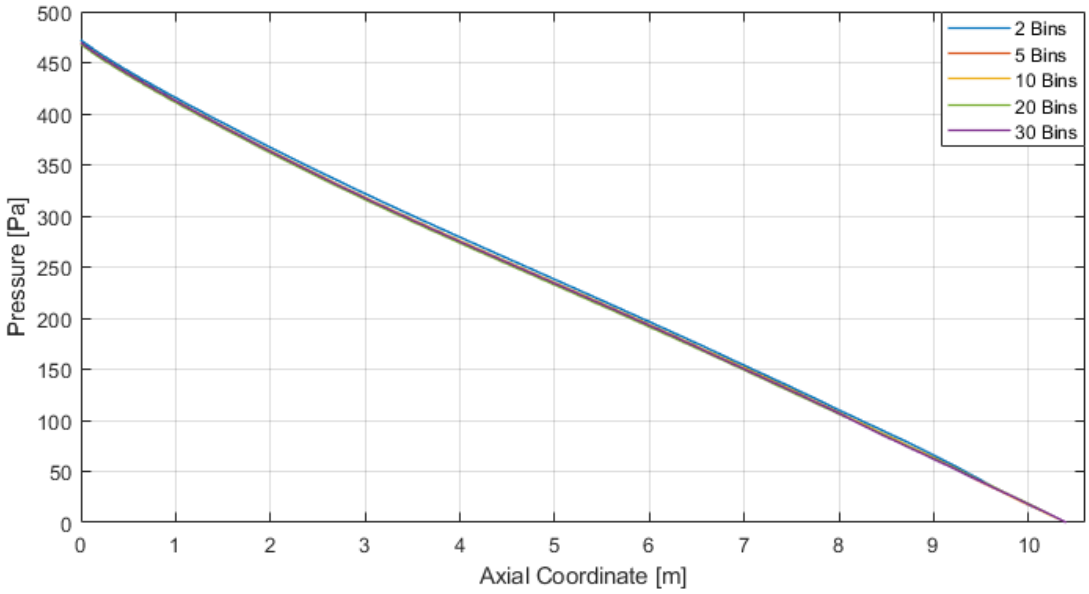

Figure 36: Pressure Drop Bin Convergence for PSD #1

The Sauter mean diameter emerged as the most effective mean diameter definition for representing the polydisperse mixture in PSD #1, yielding deviations under 1%. Quantifiable error analyses for each mean diameter expression used are presented in Table 24. Figure 37 displays the pressure drop solutions obtained for each mean diameter expression.

Table 24: Mean Diameter Analysis Compared to 30-Bin Case for PSD #1

Mean Diameter	Value (µm)	$\sqrt{\frac{1}{n}\sum_{i=1}^{n}(P_i - P_{Bin30})^2}$ (RMSD)	$\frac{\Delta P - \Delta P_{Bin30}}{\Delta P_{Bin30}} * 100$ (%)
Arithmetic Mean	250.000	1.7387	0.7621
Surface Area Mean	251.227	1.5281	0.6759
Volume Mean	252.437	1.2013	0.6241
Sauter Mean	254.874	0.281	0.2477
De Brouckere	257.243	0.4486	0.4281

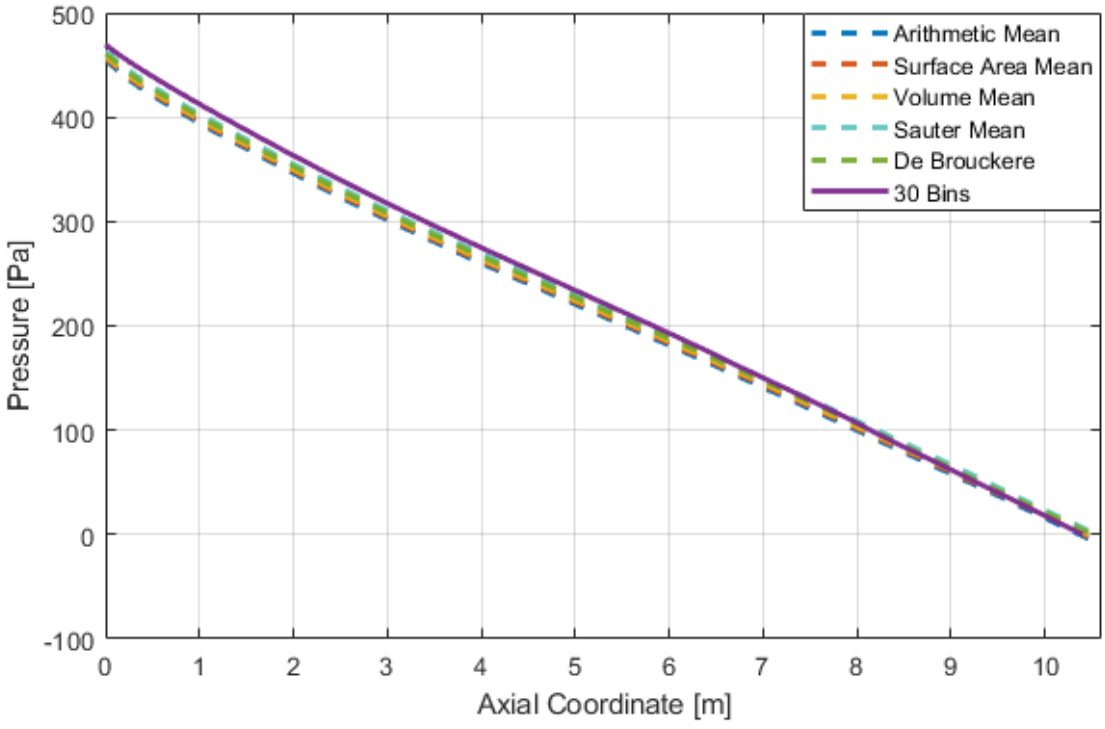

Figure 37: Pressure Drop Mean Diameter Comparison for PSD #1

ii. Particle Size Distribution Analysis #2

In the investigation of the second PSD, the ideal bin count for precise pressure drop prediction ranged from 20 to 30 bins. The bin convergence findings for the second PSD are detailed in Table 25, while Figure 38 visually presents the pressure drop solutions for each bin.

Table 25: Bin Convergence Study for PSD #2

Case	$\sqrt{\frac{1}{n}\sum_{i=1}^{n}(P_i - P_{Bin30})^2}$ (RMSD)	$\frac{\Delta P - \Delta P_{Bin30}}{\Delta P_{Bin30}} * 100$ (%)
2-Bins	5.4982	3.6896
5-Bins	3.4242	1.8465
10-Bins	2.2486	1.2221
20-Bins	1.2288	0.6341

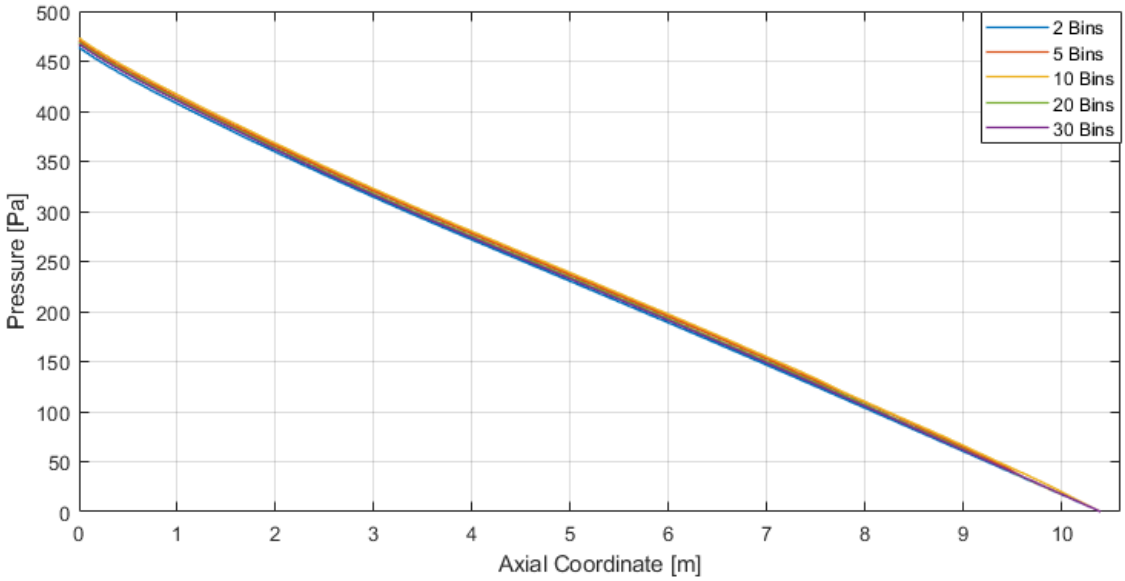

Figure 38: Pressure Drop Bin Convergence for PSD #2

The Sauter mean diameter proved to be the most efficient means of representing the polydisperse mixture in PSD #2. Detailed quantifiable error analyses for each mean diameter expression employed are provided in Table 26. Additionally, Figure 39 presents a visual representation of the pressure drop solutions obtained for each mean diameter expression.

Table 26: Mean Diameter Analysis Compared to 30-Bin Case for PSD #2

Mean Diameter	Value (μm)	$\sqrt{\frac{1}{n}\sum_{i=1}^{n}(P_i - P_{Bin30})^2}$ (RMSD)	$\frac{\Delta P - \Delta P_{Bin30}}{\Delta P_{Bin30}} * 100$ (%)
Arithmetic Mean	325.000	2.812	0.9275
Surface Area Mean	325.949	1.5814	0.7570
Volume Mean	326.889	1.5478	0.6993
Sauter Mean	327.778	0.6882	0.3484
De Brouckere	329.635	1.1793	0.5112

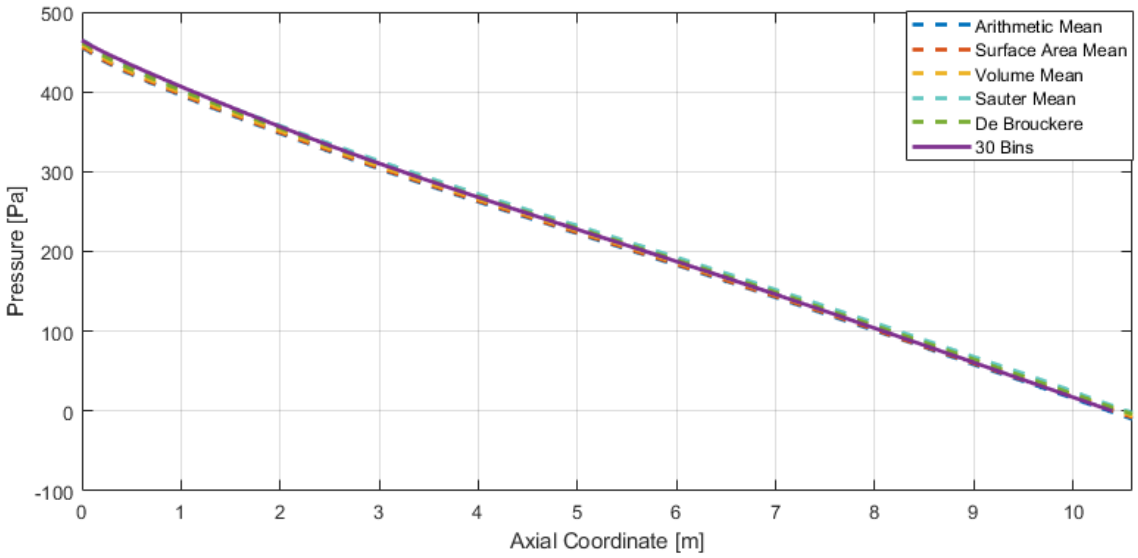

Figure 39: Pressure Drop Mean Diameter Comparison for PSD #2

iii. Particle Size Distribution Analysis #3

During the analysis of the third PSD, it was determined that the most suitable bin count for obtaining a precise pressure drop prediction without expending excessive computational resources ranged between 5 to 10 bins. Despite the fewer number of bins representing particle sizes, it was anticipated that solutions within this range would display a deviation of approximately 1%. Table 27 outlines the results of bin convergence for the initial PSD, while Figure 40 visually presents the pressure drop solutions corresponding to each bin.

Table 27: Bin Convergence Study for PSD #3

Case	$\sqrt{\frac{1}{n}\sum_{i=1}^{n}(P_i - P_{Bin30})^2}$ (RMSD)	$\frac{\Delta P - \Delta P_{Bin30}}{\Delta P_{Bin30}} * 100$ (%)
2-Bins	3.6142	1.7651
5-Bins	1.0368	0.7567
10-Bins	0.5850	0.2234
20-Bins	0.1584	0.0759

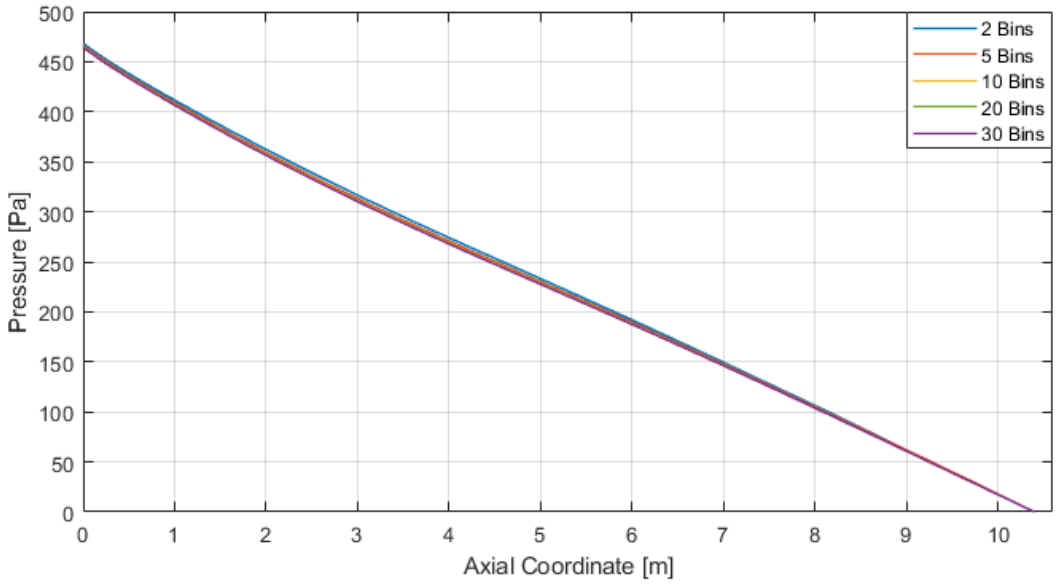

Figure 40: Pressure Drop Bin Convergence for PSD #3

The Sauter mean diameter emerged as the most effective mean diameter definition for representing the polydisperse mixture in PSD #3. Quantifiable error analyses for each mean diameter expression used are presented in Table 28. Figure 41 highlights the pressure drop solutions obtained for each mean diameter expression.

Table 28: Mean Diameter Analysis Compared to 30-Bin Case for PSD #3

Mean Diameter	Value [µm]	$\sqrt{\frac{1}{n}\sum_{i=1}^{n}(P_i - P_{Bin30})^2}$ (RMSD)	$\frac{\Delta P - \Delta P_{Bin30}}{\Delta P_{Bin30}} * 100$ (%)
Arithmetic Mean	175.000	1.5922	0.7125
Surface Area Mean	176.737	0.7144	0.4952
Volume Mean	178.426	0.5351	0.3688
Sauter Mean	181.850	0.1458	0.0856
De Brouckere	185.089	0.2603	0.1839

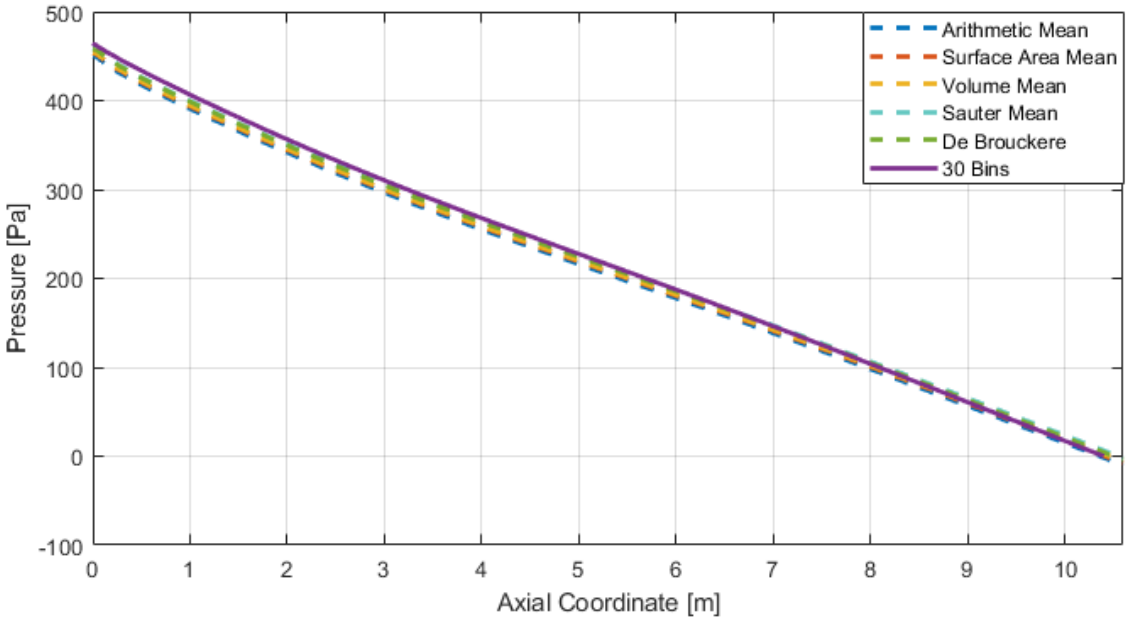

Figure 41: Pressure Drop Mean Diameter Comparison for PSD #3

iv. Particle Size Distribution Analysis #4

In the examination of the fourth PSD, the ideal bin count for precise prediction of pressure drop ranged between 10 to 20 bins. Table 29 demonstrates the outcomes of bin convergence for the initial PSD, while Figure 42 presents a visual representation of the pressure drop solutions corresponding to each bin.

Table 29: Bin Convergence Study for PSD #4

Case	$\sqrt{\frac{1}{n}\sum_{i=1}^{n}(P_i - P_{Bin30})^2}$ (RMSD)	$\frac{\Delta P - \Delta P_{Bin30}}{\Delta P_{Bin30}} * 100$ (%)
2-Bins	3.1018	1.9916
5-Bins	2.4782	1.1967
10-Bins	0.9623	0.7524
20-Bins	0.7423	0.6186

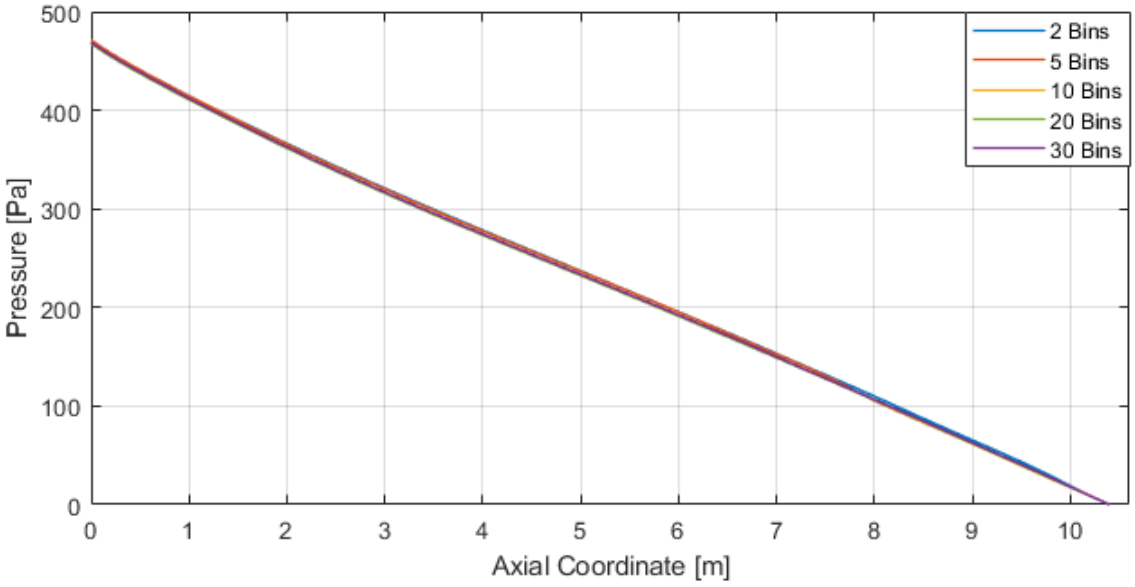

Figure 42: Pressure Drop Bin Convergence for PSD #4

The Sauter mean diameter proved to be the most effective mean diameter definition for characterizing the polydisperse mixture in PSD #4. Detailed error analyses for each mean diameter expression utilized are provided in Table 30, while Figure 43 illustrates the pressure drop solutions obtained for each mean diameter expression.

Table 30: Mean Diameter Analysis Compared to 30-Bin Case for PSD #4

Mean Diameter	Value [m]	$\sqrt{\frac{1}{n}\sum_{i=1}^{n}(P_i - P_{Bin30})^2}$ (RMSD)	$\frac{\Delta P - \Delta P_{Bin30}}{\Delta P_{Bin30}} * 100$ (%)
Arithmetic Mean	250.000	1.7451	1.5849
Surface Area Mean	257.471	0.8658	1.1280
Volume Mean	266.173	0.3640	0.7011
Sauter Mean	282.261	0.2378	0.4473
De Brouckere	294.780	0.3194	0.5888

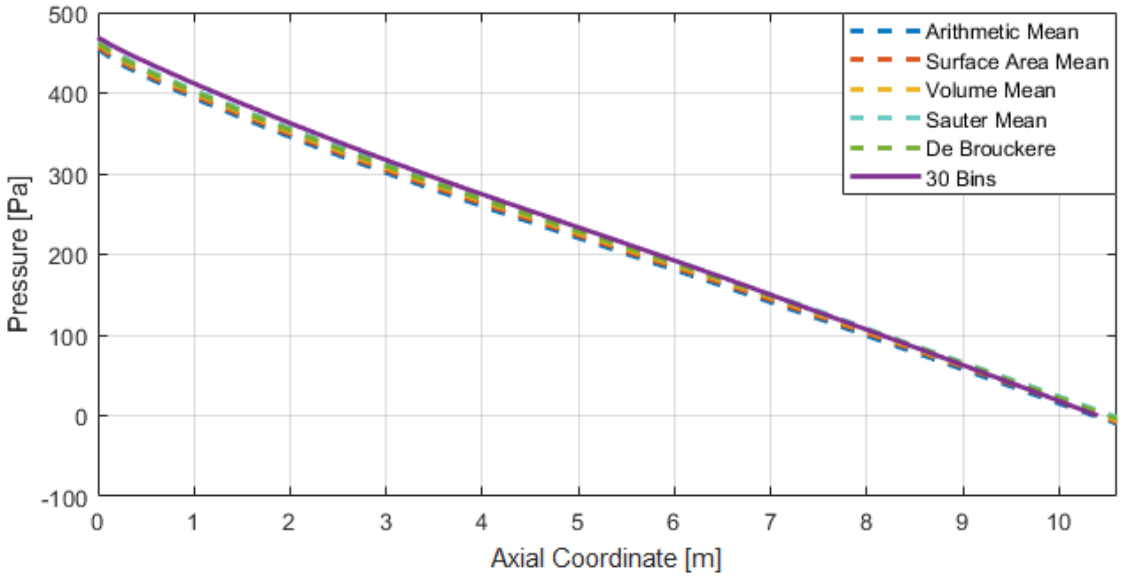

Figure 43: Pressure Drop Mean Diameter Comparison for PSD #4.

V. CONCLUSIONS

In this report, three main studies were conducted: (1) a preliminary study focused on investigating and selecting the appropriate granular models required to correctly represent the dilute flow regime in the system, (2) a study focused on validating the proposed Eulerian-Eulerian model with Laín and Sommerfeld's experimental data, and (3) a study focused on investigating the effectiveness of characterizing the polydisperse mixture using a simplified mean diameter technique. In the first study, a sensitivity analysis was performed for the proposed Eulerian-Eulerian model to select the appropriate granular property correlations necessary to describe the particulate phase, in accordance with the Kinetic Theory of Granular Flows (KTGF). From the sensitivity studies conducted and the available literature on these property models, the selected granular viscosity, temperature, and conductivity models used Gidaspow's techniques, while solids pressure and radial distribution functions used Lun et. al correlations, respectively. Other granular properties such as drag and lift coefficients were described using Wen-Yu and Saffmain-Mei correlations to fully represent the particle behavior present in the flow. To account for wall-particle interactions, the boundary conditions describing the change in granular temperature due to wall-particle interactions followed the Johnson and Jackson correlations. Since the solid phase consisted of 0.0343% of the total mixture on a volume basis and characterized a dilute flow regime, particle-particle interaction effects were found to be nearly negligible. In the second study, in addition to validating the model, an initial comparison between the polydisperse bin representation approach and monodisperse mean diameter approach was conducted. It was found that the flow data

obtained from the monodisperse case using the mean diameter from Laín's PSD agreed partially with the solutions gathered from the polydisperse bin cases and Laín and Sommerfeld's experimental data. The monodisperse mean diameter case exhibited mean differences of 4.0% in pressure drop, 4.1% in particle velocity and 40.1% in volume fraction distributions when compared to Laín's experimental data, while the highest bin case exhibited mean differences of 0.9% in pressure drop, 3.8% in particle velocity and 37.4% in volume fraction distributions. Particle velocities and volume fraction solutions were found to be more sensitive to the particle bin characterization techniques selected to represent the polydisperse mixture. In contrast, pressure drop readings exhibited lower sensitivity, displaying higher solution agreement in both monodisperse and polydisperse cases when compared with the experimental data. This second study briefly highlighted the feasibility of incorporating this simplified approach for simulating polydisperse flows to predict pressure drop within the pneumatic conveying system.

In the third study, which investigated four different arbitrary particle size distributions to determine the most suitable mean diameter correlation for accurately representing flow behavior in polydisperse mixtures, it was noted that utilizing a Sauter mean diameter led to lower pressure drop differences in overall predictions. Additionally, it was observed that bin convergence was sensitive to the particle sizes selected, with PSDs consisting of larger particle sizes requiring more bins to reach convergence compared to those with smaller particle sizes. This trend also influenced the accuracy of the mean diameter approach in representing the polydisperse mixture, as PSDs with smaller particle sizes demonstrated better agreement in pressure drop solutions between polydisperse and mean diameter monodisperse cases.

VI. FINAL REMARKS AND FUTURE DEVELOPMENT

In addition to the three main studies mentioned, future studies that would complement this investigation include exploring pressure drop effects for PSDs with larger particle size ranges. It is predicted for the solution deviation in pressure drop to keep increasing when dealing with larger particle sizes due to the increased influence the particles would have on the fluid carrier phase. The simulation could also be recreated using a transient solving scheme to investigate how particle-time dependent parameters, like particle settling time, play a larger role on pressure drop predictions. Particle velocities and volume fractions could be further analyzed using models that exhibit greater agreement with experimental data across the four established PSDs, revealing variations in solution data for these flow parameters among different cases. Lastly, integrating shape descriptors to predict particle irregularity effects in characterizing the PSD would enhance the realism of simulations for operational pneumatic conveyors. This approach could provide valuable flow data to support the development of new design and modeling strategies for these systems.

BIBLIOGRAPHY

[1] Ormer, Van, Hank (2020). *The Importance of Particle Velocity in Dilute Phase Pneumatic Conveying*. Industrial Utility Efficiency, 1-3.

[2] Bhatia, A. (2019*). Pneumatic Conveying Systems*. CFD Engineering, M05-010, 1-45

[3] Çengel, Y.A. and Cimbala, J.M. (2010). *Fluid Mechanics: Fundamentals and Applications*. Boston: McGraw Hill. 291-292.

[4] Panton, R. (2013). *Incompressible Flow*. Wiley, 4th Edition. 170.

[5] Sonin, A.A. (2001). *The Physical Basis of Dimensional Analysis*. 2nd Edition, Department of Mechanical Engineering, MIT, Cambridge. 1-57

[6] Laín, S., & Sommerfeld, M. (2013). *Characterization of pneumatic conveying systems using the Euler/Lagrange approach*. Powder Technology, 235, 764–782.

[7] Huber, N., & Sommerfeld, M. (1998). *Modelling and numerical calculation of dilute-phase pneumatic conveying in pipe systems*. Powder Technology, 99(1), 90–101.

[8] Sarrami Foroushani, A., & Nasr Esfahany, M. (2015). *CFD simulation of gas-solid two-phase flow in pneumatic conveying of wheat*. Iranian Journal of Chemistry and Chemical Engineering, 34(4), 123–140.

[9] Senapati, S. K., Mohanty, A., & Dash, S. K. (2021). *Pneumatic transport of heavy minerals in a horizontal pipe: An Eulerian-Eulerian approach*. Materials Today: Proceedings, 44, 3091–3096.

[10] Ariyaratne, W. K. H., Manjula, E. V. P. J., Ratnayake, C., & Melaaen, M. C. (2018). *CFD Approaches for Modeling Gas-Solids Multiphase Flows - A Review*. Proceedings of The 9th EUROSIM Congress on Modelling and Simulation, EUROSIM 2016, The 57th SIMS Conference on Simulation and Modelling SIMS 2016, 142, 680–686.

[11] Ding, J. and Gidaspow, D. (1990). *A Bubbling Fluidization Model Using Kinetic Theory of Granular Flow.* AIChE J., 36(4), 523–538.

[12] Zaynetdinov, K., Shah, S., Kiani-Oshtorjani, M., & Jalali, P. (2023). *Direct numerical simulations for assessment of gas-solid drag models in two-dimensional random arrays of particles*. Advanced Powder Technology, 34(1).

[13] Upadhyay, M., Kim, A., Kim, H., Lim, D., & Lim, H. (2020). *An assessment of drag models in eulerian–eulerian cfd simulation of gas–solid flow hydrodynamics in circulating fluidized bed riser*. ChemEngineering, 4(2), 1–19.

[14] ANSYS, Inc. (2021). *ANSYS Fluent Theory Manual*. 18.5, 623-742.

[15] Gidaspow, D., Bezburuah, R., & Ding, J. (1992). *Hydrodynamics of Circulating Fluidized Beds, Kinetic Theory Approach*. In Fluidization VII, Proceedings of the 7th Engineering Foundation Conference on Fluidization, 75–82.

[16] Gidaspow, D. (1994). Multiphase Flow and Fluidization. Academic Press.

[17] Ding, J., & Gidaspow, D. (1990). A Bubbling Fluidization Model Using Kinetic Theory of Granular Flow. AIChE Journal, 36(4), 523–538.

[18] Ariyaratne, W., Welahettige, P., & Melaaen, M. (2017). *A parametric study for Euler-granular model in dilute phase vertical pneumatic conveying*. The International Journal of Computational Methods and Experimental Measurements, Volume 6 (2018), Issue 1, 46-58.

[19] Johnson, P. C., & Jackson, R. (1987). *Frictional-Collisional Constitutive Relations for Granular Materials, with Application to Plane Shearing*. Journal of Fluid Mechanics, 176, 67–93.

[20] Pouraria, H., Park, K. H., & Seo, Y. (2021). *Numerical modelling of dispersed water in oil flows using eulerian-eulerian approach and population balance model*. Processes, 9(8).

[21] Kharoua, N., Khezzar, L., & Saadawi, H. (2013*). CFD Modelling of a Horizontal Three-Phase Separator: A Population Balance Approach*. American Journal of Fluid Dynamics, 3(4), 101–118.

[22] Agahzamin, S., & Pakzad, L. (2019). *A comprehensive CFD study on the effect of dense vertical internals on the hydrodynamics and population balance model in bubble columns*. Chemical Engineering Science, 193, 421–435.

[23] Laín, S., & Sommerfeld, M. (2007). *A study of the pneumatic conveying of non-spherical particles in a turbulent horizontal channel flow.* Brazilian Journal of Chemical Engineering, 24(4), 535–546.

[24] Wen, C.-Y., & Yu, Y. H. (1966). *Mechanics of Fluidization*. Chemical Engineering Progress Symposium Series, 62, 100–111.

[25] Richardson, J. R., & Zaki, W. N. (1954). *Sedimentation and Fluidization: Part I*. Transactions of the Institution of Chemical Engineers, 32, 35–53.

[26] Saffman, P. G. (1965). *The Lift on a Small Sphere in a Slow Shear Flow*. Journal of Fluid Mechanics, 22, 385–400.

[27] Mei, R., & Klausner, J. F. (1994*). Shear Lift Force on Spherical Bubbles*. Journal of Fluid Mechanics, 15, 62–65.lxxxiii

[28] Lun, C. K. K., Savage, S. B., Jeffrey, D. J., & Chepurniy, N. (1984). *Kinetic Theories for Granular Flow: Inelastic Particles in Couette Flow and Slightly*

Inelastic Particles in a General Flow Field. Journal of Fluid Mechanics, 140, 223–256.

[29] Johnson, P. C., & Jackson, R. (1987). *Frictional-Collisional Constitutive Relations for Granular Materials, with Application to Plane Shearing*. Journal of Fluid Mechanics, 176, 67–93.

[30] Tai, Y. Q., Wang, C. H., & Ray, M. B. (2005). *Dilute gas-solid flows in horizontal and vertical bends*. Industrial and Engineering Chemistry Research, 44(7).

[31] Rohatgi, A. (2022). *WebPlotDigitizer User Manual (Version 4.6)*. Automeris, 1-11.

[32] Combustible Dust Performance-Based Design Center. (2024). *Using the Particle Bin Calculator for Discrete Population Balance Models*. 1-8.

[33] Malvern. (2012). *A Basic Guide to Particle Characterization.* Malvern Instruments Worldwide, 1-24

[34] Zhong, H., Lan, X., Gao, J., Zheng, Y., & Zhang, Z. (2015). *The difference between specularity coefficient of 1 and no-slip solid phase wall boundary conditions in CFD simulation of gas-solid fluidized beds.* Powder Technology, 286, 740–743.

[35] Roenby, J., Bredmose, H., & Jasak, H. (2016). *A computational method for sharp interface advection.* Royal Society Open Science, *3*(11).

[36] Vision Analytical. (2019). *An Introduction to Particle Characterization*. AZoM Materials, 1-3.

VII. APPENDICES

A. Neglection of Virtual Mass and Turbulent Dispersion Forces

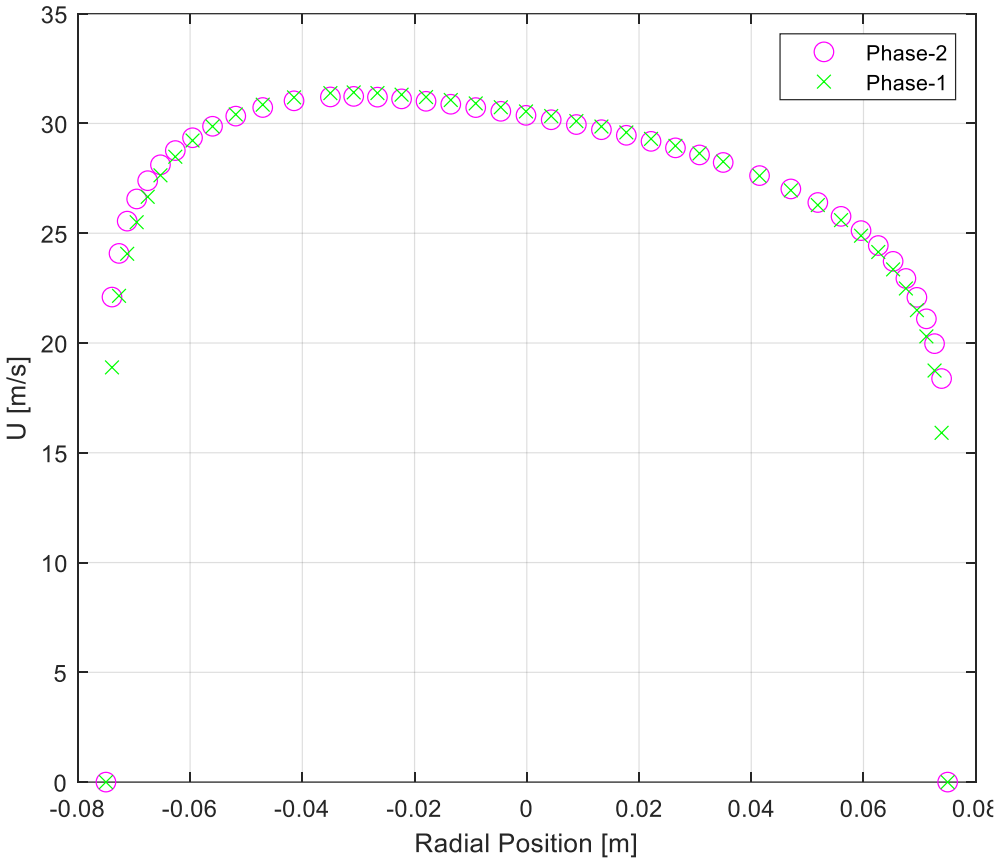

Figure A.1: Gaseous and Solid Phase Velocities for 40 µm Dilute Case.

In Figure A.1, Phase-1 represents the gaseous phase (air), while Phase-2 represents the solid phase (glass beads). As depicted, the velocities of the solid and gaseous phases exhibit a notable similarity. This similarity arises from the predominant influence of the fluid carrier phase on the particle flow. With the Stokes number within the flow

remaining below 0.1, the fluid carrier phase exerted dominant control over the motion and trajectory of the particulate phase. Because of this, the average percent difference between both velocity profiles was calculated to be 0.25463%.

Furthermore, smaller particle sizes demonstrated greater agreement in velocity profiles, particularly noticeable for particles below $100\mu m$. In contrast, agreement between phase velocities tended to decrease with larger particle sizes. This trend suggested that larger particles were more likely to move independently of the fluid carrier's influence, due to the Stokes number increasing in the flow. The absence of acceleration between phases relative to each other for the particle sizes studied allowed for the neglection of the virtual mass force term in the numerical models employed.

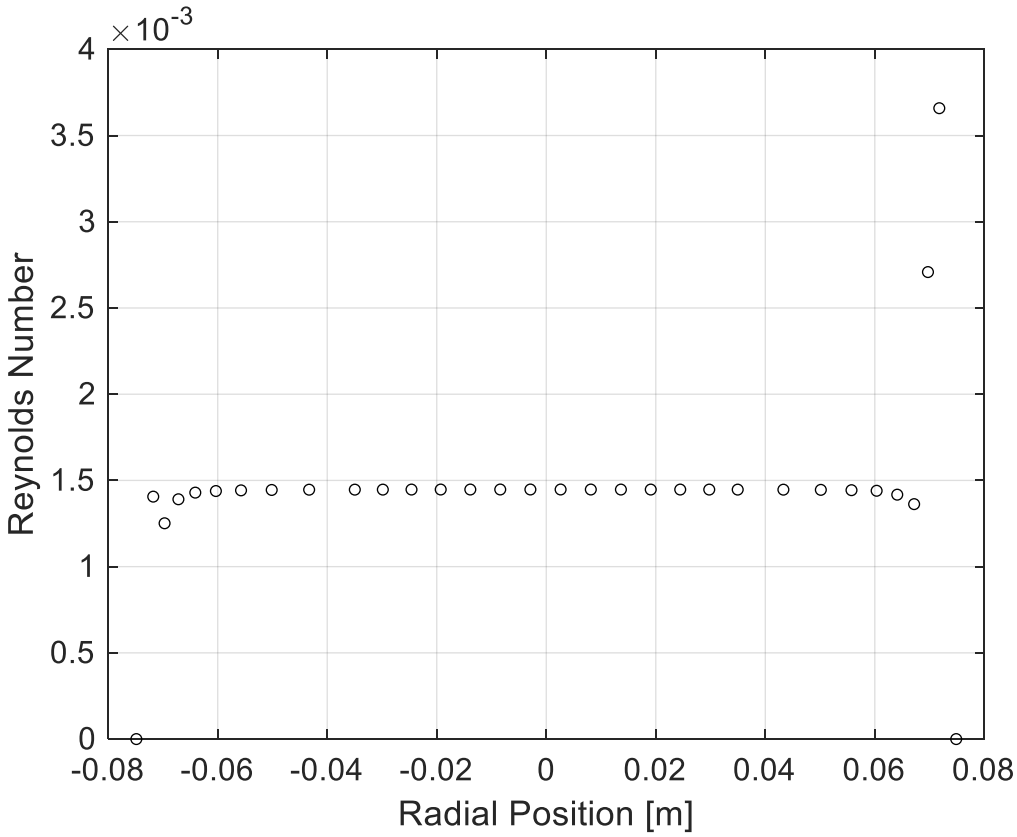

Figure A.2: Reynold's Number for 40 µm Dilute Case.

To exclude the turbulent dispersion force from the selected numerical models, it was necessary to assess the Reynolds numbers of the flows under investigation. Using Figure A.2, it was observed that the flows studied exhibited low particle Reynolds numbers. Specifically, Reynolds numbers decreased for smaller particle sizes, while they increased for larger particle sizes, consequently amplifying the error associated with neglecting the turbulent dispersion force. However, for the particle sizes examined in this study, the Reynolds numbers remained below the threshold outlined in Laín's study [23]. This justified the decision to neglect the turbulent dispersion force in the simulations.

B. Granular Models Sensitivity Studies

The sensitivity studies depicted in the following figures aimed to identify models that showed higher sensitivity to the chosen modeling scheme. These findings enabled further validation of the models documented in literature. Figure B.1 illustrates minimal disparities between the tested models, except for the volume fraction profiles for the algebraic temperature model. Given these observations, the Gidaspow model was chosen to accurately represent the granular temperature within the system.

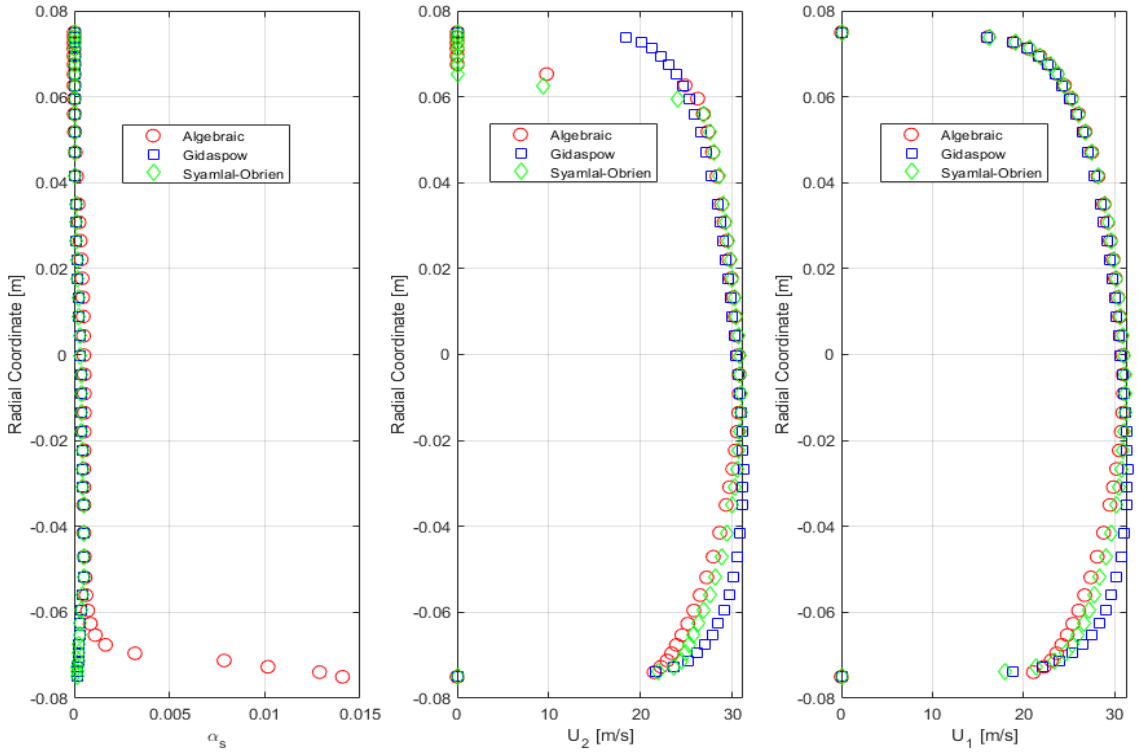

Figure B.1: Granular Temperature Modeling Comparison

Figure B.2 highlights significant agreement in volume fractions between the Gidaspow and Syamlal-Obrien models, along with disparities in velocity profiles for both the gaseous and solid phases. The utilization of the Gidaspow model facilitated the acquisition of appropriate volume fraction distributions while effectively representing the diverse velocities obtained when employing significantly different particle sizes:

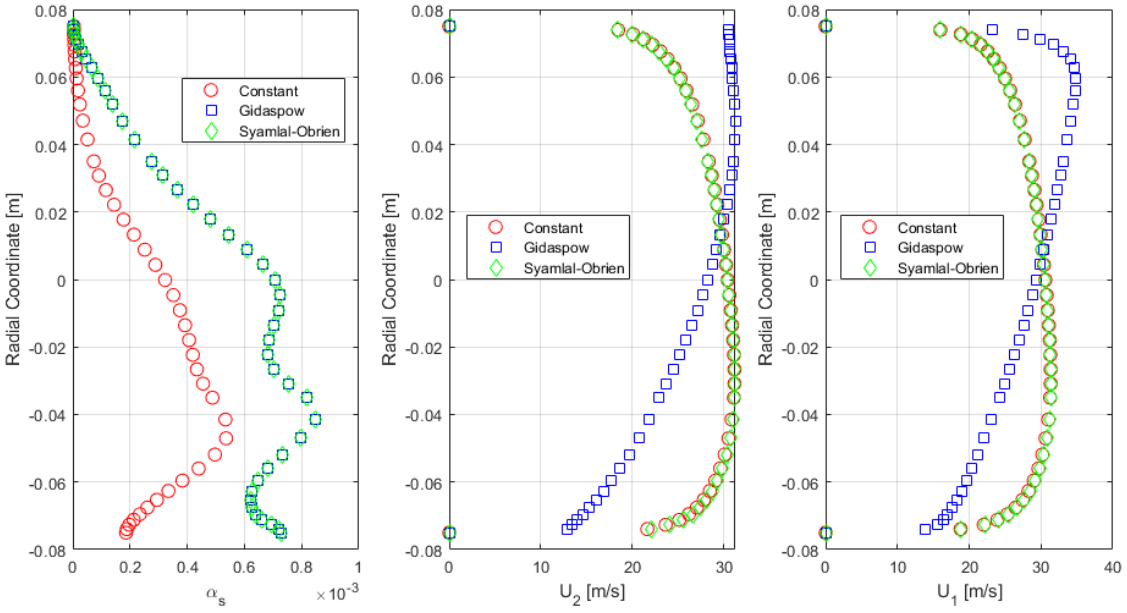

Figure B.2: Granular Viscosity Modeling Comparison

In Figure B.3 it can be observed that drag coefficient models gave rise to similar distributions across all particle properties investigated. Considering the negligible impact on solution accuracy demonstrated by these models and supported by previous studies, the Wen-Yu drag coefficient model was selected to characterize the dilute flow regime:

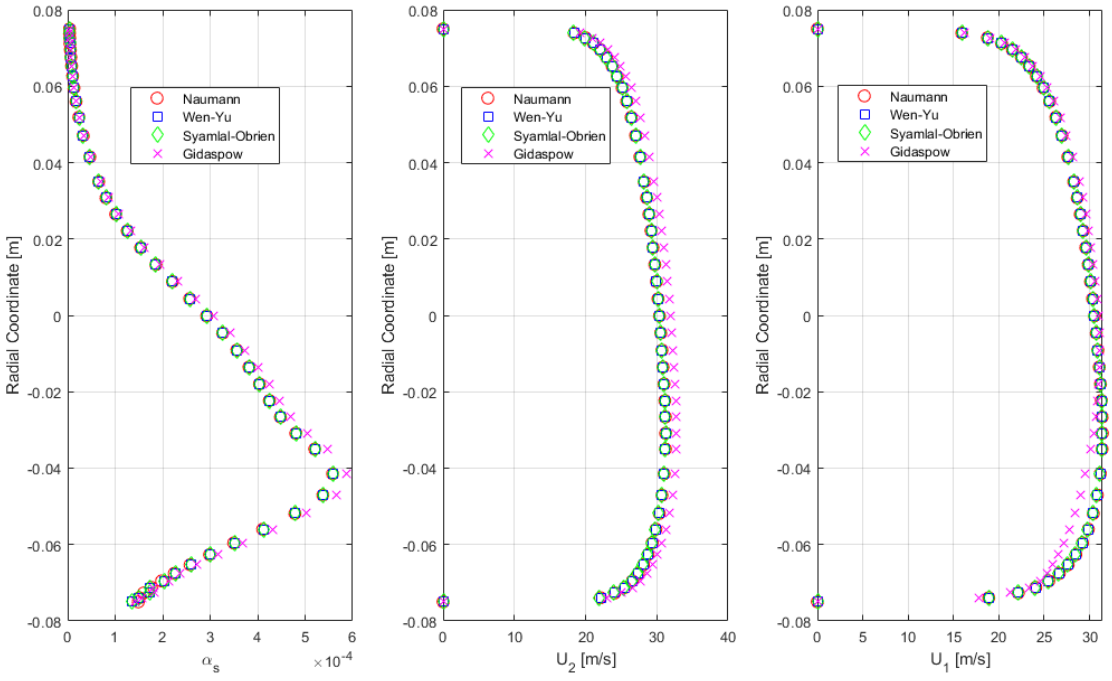

Figure B.3: Drag Coefficient Modeling Comparison

Figure B.4 shows that the boundary value selected to describe the particulate phase inlet granular temperature had a negligible effect on solution accuracy. Based on these findings, the granular inlet temperature was selected to be $0.0001 \frac{m^2}{s^2}$:

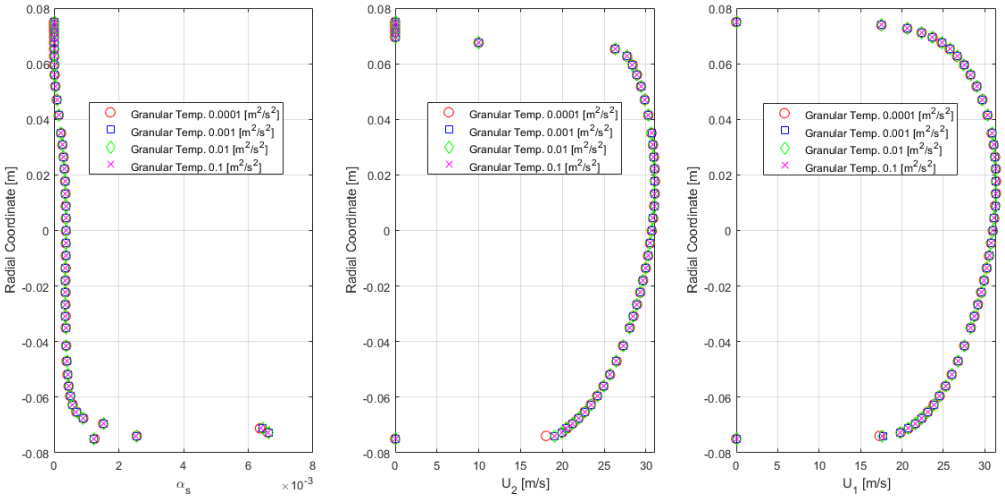

Figure B.4: Inlet Granular Temperature Modeling Comparison

When investigating solids pressure and radial distribution function models, the Lun et. al and Syamlal-Obrien model combinations were investigated. Both models showed comparable results. Given the negligible difference in solution accuracy and to keep consistency with previous literature, the Lun et. al model was selected to describe these parameters:

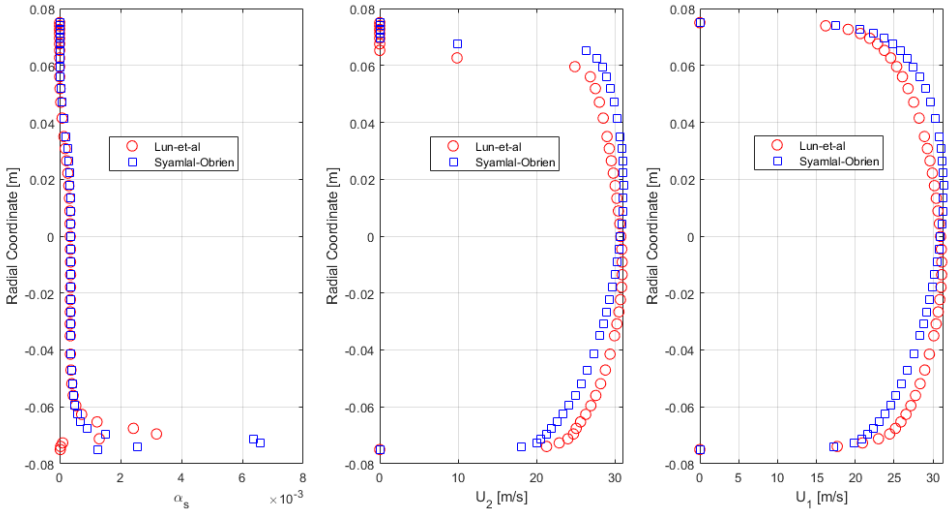

Figure B.5: Solids Pressure and Radial Distribution Modeling Comparison.